Technical Report
TR-17-11
June 2018

Bentonite swelling into fractures at conditions above the critical coagulation concentration

Lennart Börgesson
Magnus Hedström
Martin Birgersson
Ola Karnland

SVENSK KÄRNBRÄNSLEHANTERING AB

SWEDISH NUCLEAR FUEL
AND WASTE MANAGEMENT CO

Box 3091, SE-169 03 Solna
Phone +46 8 459 84 00
skb.se

ISSN 1404-0344
SKB TR-17-11
ID 1603316

June 2018

Bentonite swelling into fractures at conditions above the critical coagulation concentration

Lennart Börgesson, Magnus Hedström,
Martin Birgersson, Ola Karnland
Clay Technology AB

This report concerns a study which was conducted for Svensk Kärnbränslehantering AB (SKB). The conclusions and viewpoints presented in the report are those of the authors. SKB may draw modified conclusions, based on additional literature sources and/or expert opinions.

A pdf version of this document can be downloaded from www.skb.se.

© 2018 Svensk Kärnbränslehantering AB

Abstract

Swelling of bentonite into a fracture that takes place in a groundwater that has a NaCl concentration above the critical coagulation concentration (CCC) has been analysed. The processes involved when bentonite swells until it becomes a non-swelling gel, which it will when the groundwater is above the CCC, have been analysed. Since the problem of colloid erosion is largest for homoionic Na-montmorillonite, limits have been determined for such types of systems. CCC for homoionic Na-montmorillonite (Wy-Na) extracted from MX-80 is circa 20 mM NaCl(aq). At this NaCl concentration the swelling stops at a clay concentration of approximately 60 g/L.

In order to estimate the swelling of bentonite in a fracture we need to know

- the swelling pressure and swelling behaviour of the bentonite at clay concentrations higher than 60 g/L,
- the resistance against penetration that is caused by shear resistance or friction in the bentonite and between the bentonite and the fracture surfaces and
- the shear strength of the non-swelling gel at 60 g/L.

In addition we need to have a calculation tool for estimating the penetration depth and the swelling pressure and density loss along the fracture. These things have been investigated and analysed in this report.

The common tests and expressions of swelling pressure have concerned higher densities than the density of a maximum swollen bentonite gel near the CCC. In order to include lower densities DLVO theory and DLVO theory combined with literature swelling pressure data at low clay concentrations have been used to derive expressions of swelling pressure vs dry density. The DLVO pressure at 60 g/L and 20 mM NaCl is virtually negligible while the expression that also incorporates experimental information gives a pressure of about 1 kPa. Since the clay is a non-swelling gel at the CCC at 60 g/L the pressure is explicitly set to 0 for lower clay concentrations at CCC.

Another issue concerns the shear strength of the non-swelling gel. With rotating-vane rheometry the shear strength at CCC and 60 g/L was determined to be 40 Pa for a gel that has been left undisturbed for 44 h. It was shown that this value is far higher than expected shear stresses that the gel may be exposed to from flowing water in a fracture. Thus, when a gel is formed no erosion is expected. This also agrees with the absence of erosion in previous tests in using flow in artificial fractures above CCC.

Theory is developed for the bentonite penetration into a horizontal fracture. The penetration depth is analysed in terms of the equilibrium situation where the swelling is completed, and the swelling pressure is balanced by the friction against the fracture walls. There are several ways of estimating the friction angle at the low dry densities relevant for the non-swelling gel. Depending on the approach taken and the swelling pressure chosen the evaluated friction angles show large variations, 0.5 to 30°. However, by using these large variations in the sensitivity analyses we were able to show that the penetration into a 100 μm wide fracture is anyway limited to < 80 mm at the lowest friction angle. Comparison between theory and experimental swelling of Wy-Na into a 120 μm fracture gives best agreement for the highest friction angle, 30° which gave a penetration depth in the vicinity of 1 mm. Other examples of measurements of swelling clays both above and below CCC confirm that the depth of swelling of a gel into a fracture is very small. Thus, we can conclude that above the CCC the bentonite swelling into fractures is limited to distances very much smaller than the deposition hole diameter.

The influence of gravity was also studied and shows to be insignificant for the current problem where the salinity is above the CCC. Thus, the analysis performed for horizontal fractures also holds for sloped fractures.

There are numerous examples of measurements of shear resistance in bentonite and between bentonite and a surface. In the report examples are given of both finished and ongoing measurements, which show that complete homogenisation is hindered by frictional stresses in the bentonite and

between the bentonite and the confining surfaces. Ten long-term tests in long tubes are ongoing with low density bentonite in one half of the tube in contact with high density bentonite in the other half. The most long-lasting test has been running for 5 years. One test was terminated after two years. Both show a remaining density gradient in the axial direction that corresponds to an average friction angle between the bentonite and the tube of about 7 degrees. The remaining tests are planned to continue for many years and be terminated and sampled successively.

Creep tests with constant deviatoric stress applied on a bentonite specimen in a triaxial apparatus have shown that the creep rate decreases very fast and cannot give rise to large deformations and loss of shear resistance.

In conclusion this report shows that there is a shear resistance or a friction in bentonite and between bentonite and confining surfaces that hinders bentonite to swell deeply into any fracture in a groundwater with salinity above the CCC. In addition the report shows that the strength of the non-swelling bentonite gel that is formed at the swelling front is with large margin high enough to withstand both the gravitational forces and the erosional forces caused by ground water flow past the swelling front.

Sammanfattning

Utsvällning av bentonit i en spricka som äger rum i ett grundvatten som har en NaCl-koncentration över den kritiska koaguleringskoncentrationen (CCC) har studerats. De processer som medverkar när bentonit sväller tills den blir en icke-svällande gel, vilket blir resultatet när grundvattnet ligger över CCC, har analyserats. Eftersom problem med kolloiderosion från bentonit är störst för homojonisk Na-montmorillonit (Wy-Na) har gränsvärden bestämts för sådana system. CCC för Na-bentonit utvunnet från MX-80 (Wy-Na) är ca 20 mM NaCl(aq). Vid den NaCl-koncentrationen slutar leran att svälla vid en lerkoncentration av ungefär 60 g/L.

För att kunna uppskatta hur en bentonit sväller in i en spricka behöver vi ha kunskap om

- svälltryck och svällningsegenskaper hos bentonit vid lerkoncentrationer högre än 60 g/L,
- det motstånd mot utsvällning som orsakas av skjuvmotstånd eller friktion i bentoniten och mellan bentoniten och sprickytorna, och
- skjuvhållfastheten hos den icke-svällande gelen vid 60 g/L.

Dessutom behövs ett beräkningsverktyg för att uppskatta inträngningsdjupet och svälltrycks- och densitetsförlusten längs sprickan. Erforderliga materialdata har tagits fram och utträngningsberäkningar har gjorts och redovisas i denna rapport i kombination med känslighetsaspekter och osäkerheter.

De vanligaste svälltryckstesterna och sambanden för svälltryck har avsett högre densiteter än densiteten vid maximal utsvällning nära CCC. För att även beskriva lägre densiteter har DLVO-teori kombinerat med litteratur med svälltrycksdata vid låga lerkoncentrationer använts för att ta fram samband mellan svälltryck och torrdensitet. Det DLVO-beräknade svälltrycket vid 60 g/L och 20 mM NaCl är försumbart, emedan uttryck som också innehåller experimentella data ger svälltryck kring 1 kPa. Eftersom leran är icke-svällande vid CCC och en lerkoncentration på 60 g/L sätts svälltrycket till noll vid lägre koncentrationer.

En annan fråga gäller skjuvhållfastheten hos den icke-svällande gelen. Skjuvhållfastheten hos gelen vid CCC och 60 g/L har bestämts med en roterande vinge efter olika vilotid. Efter 44 timmars vila uppmättes en skjuvhållfasthet på 40 Pa. Detta värde är mycket högre än de förväntade skjuvspänningarna orsakade av flödande vatten i sprickorna. Ingen erosion kan alltså förväntas efter det att den icke-svällande gelen har bildats. Detta stämmer också överens med avsaknaden av erosion i utförda tester i konstgjorda sprickor.

En teori har utvecklats avseende bentonitinträngning i plana horisontella sprickor. Teorin ger sluttillståndet vid jämnvikt när svällningen är avslutad och svälltrycket balanserats av friktion mot sprickväggarna. Det finns flera sätt att uppskatta friktionsvinkeln vid de låga densiteter som är relevanta för en icke svällande gel. Beroende på hur man angriper problemet och vilket svälltryck som används kan den utvärderade friktionsvinkeln variera mellan 0.5° och 30°. Trots dessa ytterligheter visar en känslighetsanalys att utträngningen i en spricka med aperturen 100 μm blir högst 80 mm. Jämförelse mellan teoretiska och experimentella resultat avseende utträngning av Wy-Na i en 120 μm spricka gav bäst överensstämmelse för den höga friktionsvinkeln 30°, då utträngningen blev ungefär 1 mm. Andra exempel på mätningar på svällande lera, både under och över CCC, bekräftar att det djup som en gel sväller in i en spricka är mycket litet. Vi kan alltså dra slutsatsen att bentonitutträngning i sprickor under förhållanden över CCC begränsas till avstånd som är mycket mindre än diametern på deponeringshålet.

Påverkan av gravitationen har också studerats. Resultaten visar att gravitationens inverkan på sprickutträngning är försumbar för förhållanden över CCC. Analysen avseende horisontella sprickor gäller alltså även lutande sprickor.

Det finns otaliga exempel på uppmätt skjuvmotstånd i bentonit och mellan bentonit och begränsningsytor. I rapporten ges exempel på både avslutade och pågående mätningar, vilka alla visar att fullständig homogenisering förhindras av friktionsrelaterade spänningar i bentoniten och mellan bentoniten och begränsningsytorna. Tio långtidsförsök i långa rör pågår med bentonit med låg densitet i ena halvan av röret som står i kontakt med bentonit med hög densitet i andra halvan.

Det äldsta försöket har gått i fem år. Ett försök bröts efter två år. Båda dessa försök visar på en kvarstående densitetsgradient i axiell riktning som motsvarar en medelfriktionsvinkel mellan bentoniten och röret på ungefär 7 grader. Försöken ska fortgå i många år och brytas och provtas succesivt.

Krypförsök, som utförts med en konstant deviatorspänning applicerad på ett bentonitprov i en triaxialcell, visar att kryphastigheten snabbt avtar och inte kan ge upphov till stora deformationer och förlust av skjuvmotstånd.

Sammanfattningsvis har denna rapport visat att det finns ett skjuvmotstånd eller friktion i bentonit och mellan bentonit och dess begränsningsytor som förhindrar att bentonit sväller djupt in i varje spricka då grundvatten har en salthalt som överstiger CCC. Dessutom visas att skjuvhållfastheten hos den icke-svällande bentonitgelen som bildas vid svällningsfronten med stor marginal är tillräckligt hög för att motstå både inverkan av gravitationen och de erosionskrafter som orsakas av ett grundvattenflöde i kontakt med svällningsfronten.

Contents

1 **Introduction** 9

2 **Basic properties of bentonite at low densities** 11
2.1 General 11
2.2 Swelling pressure of MX-80 bentonite at low densities 12
2.3 Shear strength of MX-80 close to CCC 15

3 **Hydromechanical models of swelling bentonite** 19
3.1 General 19
3.2 The effective stress theory 19
3.3 Swelling pressure and swelling properties 20
3.4 Shear resistance 21
  3.4.1 General 21
  3.4.2 Material models 22
  3.4.3 Friction angle and the dependency on the normal stress 22

4 **Swelling into a plane fracture** 25
4.1 Introduction 25
4.2 Theory 25
4.3 Calculated fracture penetration 26
4.4 Comparison with measurements 27
4.5 Influence of gravity 29
4.6 Discussion and conclusions 31

5 **Proof of existence of shear resistance or friction** 33
5.1 General 33
5.2 Homogenisation of bentonite in long tubes 33
5.3 Creep of bentonite measured in triaxial cells 36
5.4 Conclusions 37

6 **Shear stresses from water flow past a bentonite gel in a fracture** 39

7 **Conclusions** 41

References 43

Appendix 1 Equilibrium after swelling into the slot without considering in-plane stresses 45

1 Introduction

The objective of this report is to investigate the behaviour of the buffer material in a deposition hole in contact with a fracture in the surrounding rock when the chemistry of the groundwater is above the critical coagulation concentration CCC of the bentonite. The reference bentonite MX-80 is considered and the ability of the bentonite to penetrate fractures and the risk of losing bentonite by erosion at the penetration front is investigated.

The report at first describes the basic properties of bentonite at low densities close to the CCC with focus on the swelling pressure and the shear strength. Then some models of the hydro-mechanical properties of bentonite are described. These models are based on laboratory measurements extrapolated to very low densities in combination with some theoretical models. In Chapter 4 a theory that describes the penetration of a swelling clay into a plane fracture is described and used to make a sensitivity analysis of the penetration depth at different possible variations of parameters included in the model. The results are compared to some measurements. In addition the influence of gravity in inclined fractures is studied.

In Chapter 5 the existence of shear resistance in a swelling bentonite is proven with examples of long term measurements and creep tests. Then the risk of erosion by water flowing past the bentonite penetration front in a fracture is analysed. Finally the results are analysed and the conclusion drawn that there will be no significant loss of bentonite from fractures intersecting the deposition hole when the chemical conditions of the ground water are above the CCC for the bentonite.

The deposition holes and the tunnels in a repository of KBS-3 type will be located at about 500 m depth in crystalline rock and filled with bentonite dominated by montmorillonite. The bentonite installed in the deposition holes and tunnels will be compacted to high density. If an open water-bearing fracture intersects the deposition hole or tunnel, bentonite will swell and to some extent expand into the fracture. During the swelling, the high density bentonite will become increasingly inhomogeneous in the fracture due to frictional forces in the bentonite and between the bentonite and the fracture walls. The swelling into the fracture will continue until the density of the bentonite has decreased to such low density that the swelling ability of the clay is lost and the clay has become a non-swelling gel or a sol. If the clay front in the fracture becomes a non-swelling gel there will be no further expansion of the bentonite into the fracture unless there are water flow of such flow rate that the shear resistance of the gel is exceeded and clay particles are dragged with the water. If the clay front becomes a sol the swelling may continue in a presently not very well known way.

This report deals with the processes involved when bentonite swells into a fracture until it becomes a non-swelling gel. This occurs when the clay is above the critical coagulation concentration (CCC). Since the problem of colloid erosion from bentonite is largest for homoionic Na-montmorillonite, limits will be determined for such types of systems. Thus the CCC is defined as the limit of the NaCl concentration in the ground water when the clay turns into a non-swelling gel instead of a sol at swelling. This conversion takes place at a clay concentration (or dry density of the clay) that can be determined. CCC for homoionic Na-montmorillonite (Wy-Na) extracted from MX-80 is circa 20 mM NaCl(aq). At this NaCl concentration the swelling stops at the clay concentration of approximately 60 g/L (Hedström et al. 2016).

2 Basic properties of bentonite at low densities

2.1 General

In this chapter the basic properties of bentonite at low densities close to the CCC are described with focus on the swelling pressure and the shear strength.

Different processes that can be modelled with different mathematical formulations are present during the transport of bentonite in a fracture system. The processes involved below CCC are very complicated and to some extent unknown. However, above CCC (circa 20 mM NaCl for Wyoming-Na) the swelling stops at a clay concentration of about 60 g/L as shown in the phase diagram in Figure 2-1 (Hedström et al. 2016). As seen in the figure the limit between when the swelling clay turns to non-swelling is depending on the salt concentration. At higher salt concentrations the transition takes place at higher clay concentrations. However, for the tested NaCl concentrations below 20 mM no gel was observed, irrespective of clay concentration.

The paste-like condition of the bentonite characterized by swelling ability at higher densities (clay concentrations) has swelling properties that are not well known. Michot et al. (2004) studied the osmotic pressure of montmorillonite slurries and pastes with clay concentrations below 50 g/l and salinity below the CCC. However, for pastes above 60 g/l there are to our knowledge few or no swelling pressure data. These low density properties are instead analysed theoretically and expressions for swelling pressure are derived in Section 2.2 below. At even higher densities (400 kg/m^3 and above) the properties are well known and the models used for modelling swelling and homogenisation of the buffer and backfill can be used.

To estimate and/or evaluate the swelling of bentonite into fractures one needs knowledge of the swelling pressure and the resistance of the bentonite against extrusion, which is caused by the internal shear resistance or friction in the bentonite and the friction between bentonite and the fracture surfaces. Swelling-pressure curves have been determined in the past for high and intermediate dry densities. To study the extrusion of bentonite one also needs the swelling pressure at low densities all the way down to the density where the gel is formed at the CCC. In Section 2.2 the swelling pressures at low densities are discussed and a semi-empirical swelling pressure curve is developed that in an approximate way aim to account for the discrepancy between DLVO theory and measured osmotic pressures.

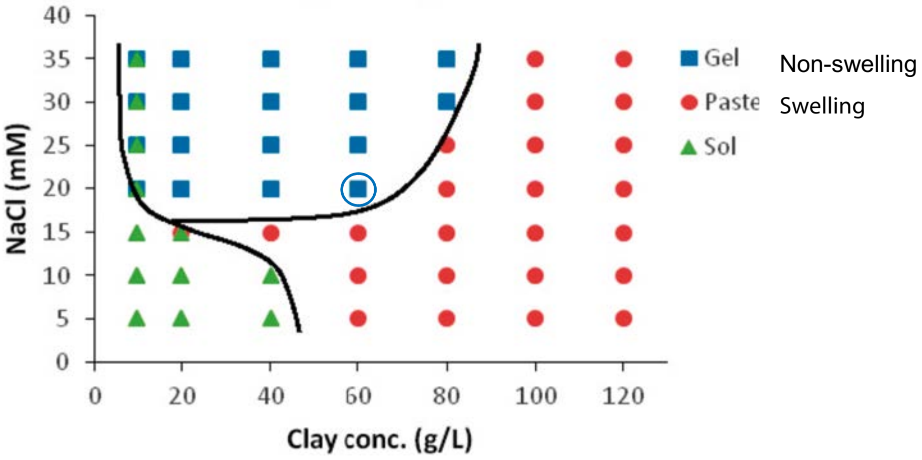

Figure 2-1. *State diagram of Wy-Na montmorillonite (TR-15-07). The gel is characterized by non-swelling properties and the paste by swelling properties.*

In Section 2.3 new measurements of the shear strength of Wy-Na at clay concentrations of 50, 60 and 70 g/l are presented. Measurements are done both at salt-free conditions and with 20 mM NaCl. The salt-free conditions gives the shear strength of the clay that still have swelling potential. Those values are used for estimating the friction angle used together with the effective stress theory, discussed in Chapter 3. The shear stress of the clay at the CCC are needed to judge if the clay gel is resilient enough to withstand the expected shearing forces from the flowing water in the fracture.

2.2 Swelling pressure of MX-80 bentonite at low densities

It is well established that the DLVO theory (Verwey and Overbeek 1948) for parallel charged layers gives a quantitatively good description of the osmotic (swelling) pressure in Li- and Na- montmorillonite at intermediate dry densities and sub-molar salinities (Karnland et al. 2005, Quirk and Marčelja 1997, Zhang et al. 1995). At high dry densities, i.e., at short montmorillonite layer separations, measured swelling pressures are higher than DLVO predictions. At such dry densities, the molecular nature of water and ions, which is not included in DLVO, gives rise to additional hydration forces (Ruths and Israelachvili 2008). Of even greater importance for the colloidal-sol-formation problem is the deviation from DLVO at very low dry densities. Again, the measured osmotic pressures are higher and much less sensitive to excess salt than the DLVO estimates (Martin et al. 2006, Michot et al. 2004, Mourchid et al. 1995). This is illustrated in Figure 2-2 where experimental data for Wyoming Na-montmorillonite at 0.01 and 10 mM NaCl is compared to calculated pressures from DLVO theory. There is a reasonably good agreement for the salinity of 0.01 mM but for 10 mM the DLVO prediction is completely wrong. The comparison to experimental data in Figure 2-2 shows that DLVO theory gives too low swelling pressures at these clay concentrations and at salinities below the CCC. In view of these results, erosion rates based on DLVO predictions will be underestimated. However, as the present report concerns the penetration of bentonite into fractures with salinities above the CCC, the results in Figure 2-2 are of less concern. Previously, it has been found that Wy-Na (Homoionic Na-montmorillonite from MX-80) does not swell beyond 60 g/l when the salinity is above the CCC ≈ 20 mM NaCl (Hedström et al. 2016). Thus in the computations herein, swelling pressure is assumed to be zero for clay concentrations < 60 g/l to conform with the experimental evidence. Two expressions for the swelling pressure will be 'derived'. One that is a fit to DLVO at 20 mM salinity and one that is a semi-empirical compromise between the DLVO at 20 mM and the data in Figure 2-2.

First we discuss the semi-empirical expression. At higher dry densities the pressure should be close to the DLVO expression for Na-montmorillonite at NaCl concentration of 20 mM while at lower dry densities we try to incorporate the fact that experimental pressures are larger than the DLVO prediction. This is done by using the DLVO pressure at 1 mM and dry density $\rho_d = 50\ \text{kg/m}^3$ in the fit. At the same time the aim has been to reduce the number of fitting parameters so for dry densities $\rho_d < 700\ \text{kg/m}^3$ we assign a power dependence of pressure on ρ_d. Such a simple expression cannot perfectly fit the 1 mM condition at $\rho_d = 50\ \text{kg/m}^3$ and also asymptotically the 20 mM curve.

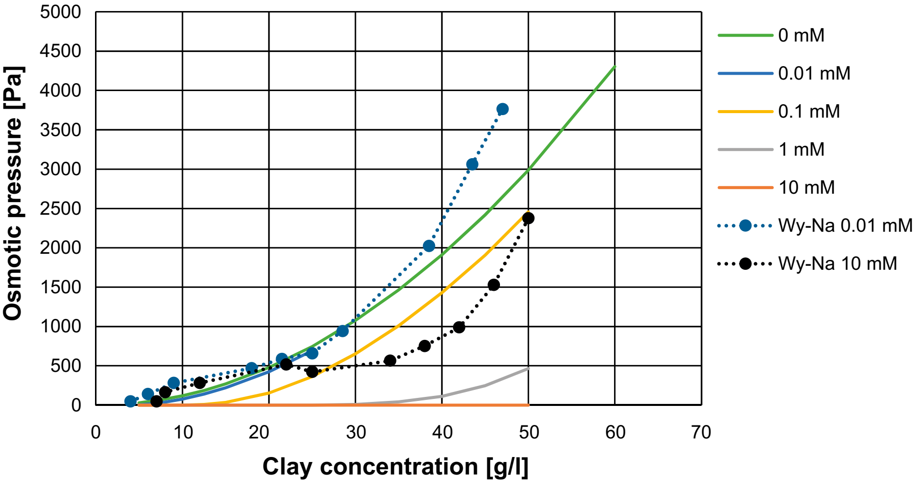

Figure 2-2. Comparison between experimental osmotic pressure data (markers connected with dotted lines) (Michot et al. 2004) and calculated pressures from DLVO theory (smooth lines).

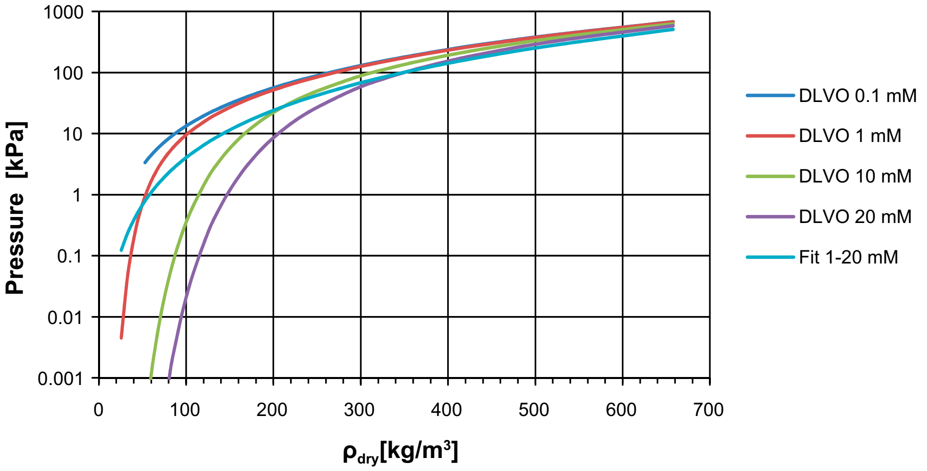

Figure 2-3. *Swelling pressure from DLVO theory and a semi-empirical fit (Fit 1–20 mM).*

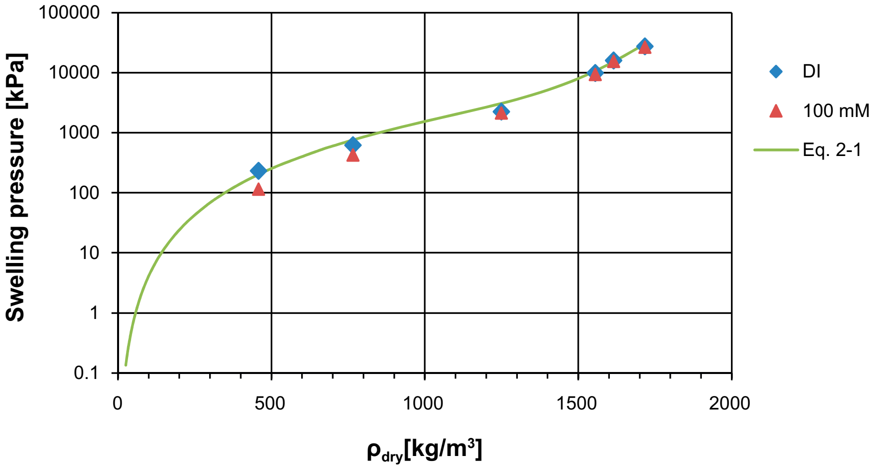

Figure 2-4. *Swelling pressure using a power law and exponential dependence of dry density to fit DLVO results for 20 mM at intermediate density and experimental findings at low and high dry densities. Data for Wy-Na from Karnland et al. (2006) and solid line from Equation 2–1.*

The semi-empirical pressure is given by

$$\sigma_s(\rho_d) = 0.0094 \cdot \exp(0.0086 \cdot \rho_d) + 3 \cdot 10^{-5} \cdot \rho_d^{2.5656} \text{ [kPa]} \qquad \text{(Equation 2–1)}$$

At $\rho_d \approx 50$ kg/m^3 it crosses the 1 mM DLVO curve and at $\rho_d > 300$ kg/m^3 it approaches the DLVO curve for 20 mM NaCl as can be seen in Figure 2-3. In fact the difference in DLVO pressure for 0.1 mM NaCl and salinities up to 20 mM are becoming smaller and smaller as ρ_d increases. The exponential function in Equation 2–1 is fitted to the experimental data at high dry density, and describes the effect of hydration not included in DLVO. Figure 2-4 shows how σ_s performs over the whole dry density range. Note also that the experimental data for deionized (DI) water and 100 mM NaCl essentially overlap for $\rho_d > 1\,200$ kg/m^3.

Equation 2–1 is not meant to capture the behaviour of Wy-Na at clay concentrations < 60 g/l because of coagulation, which represents a phase transition. This experimental fact will have to be taken into account explicitly by setting $\sigma_s = 0$ for $\rho_d < 60$ kg/m^3.

For comparison we also parameterize the DLVO results for 20 mM NaCl and also include the effect of hydration at high dry density. The DLVO calculations were done assuming a clay layer thickness of 9.3 Å and a Hamaker constant of 2.2×10^{-20} J and a negative surface charge density corresponding to 140 Å^2/*e*. At $\rho_d < 700$ kg/m^3, the weak overlap approximation to the Poisson-Boltzmann equation is valid, thus we fit a function of the form $C \cdot exp(-D(\rho s/\rho d - 1))$ to the DLVO results (Evans and Wennerström 1999). The resulting equation, where also the experimental data at $\rho_d > 1\,500$ kg/m^3 is taken into consideration, is

$$\sigma_s^{DLVO}(\rho_d) = f_{cut}(\rho_d) \cdot Ae^{B\rho_d} + C \cdot e^{-D(\rho_s/\rho_d - 1)} \quad \text{(Equation 2–2)}$$

where $A = 0.1097$ kPa, $B = 0.0072$ m^3/kg, $C = 2\,279.3$ kPa, and $D = 0.4371$ are adjusted to fit the experimental data for $\rho_d > 1\,500$ kg/m^3 (*A* and *B*) and the DLVO results (*C* and *D*) for $\rho_d < 700$ kg/m^3. The grain density, $\rho_s = 2\,780$ kg/m^3, and f_{cut} is a sigmoidal cut-off function applied to the high dry density term and is given by

$$f_{cut}(\rho_d) = \left(1 + \exp\left(-8(\rho_d/800 - 1)\right)\right)^{-1} \quad \text{(Equation 2–3)}$$

The swelling pressure expression in Equation 2–2 gives a perfect fit to the DLVO results below dry densities of 800 kg/m^3 as shown in Figure 2-5. This confirms that the weak overlap approximation is valid and it also shows that the effect of van der Waals interaction (Hamaker treatment) is virtually negligible for $\rho_d < 700$ kg/m^3. It is also evident that the DLVO expression underestimates the swelling pressure at high dry densities.

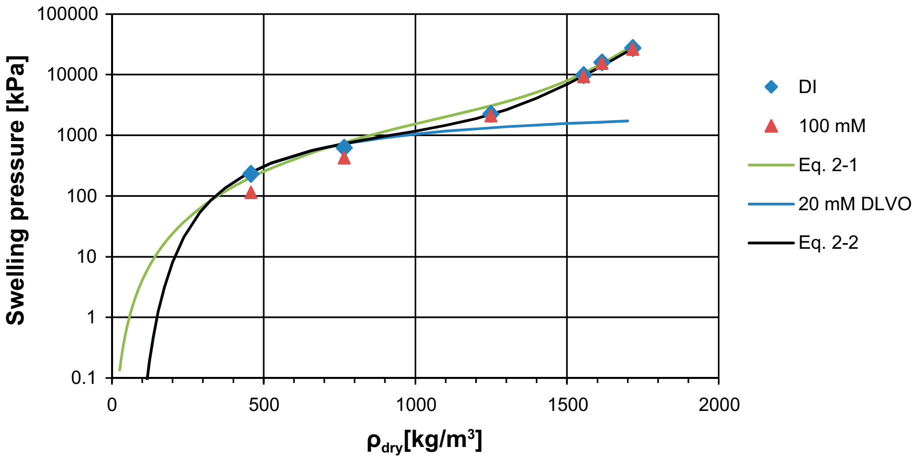

***Figure 2-5.** Comparison of different expressions for swelling pressure. Black curve (Equation 2-2) fit the 20 mM DLVO results below dry densities of 800–1 000 kg/m^3 and the experimental data at high dry densities. At low ρ_d the swelling pressure from DLVO theory at 20 mM is significantly lower than the pressure from Equation 2-1.*

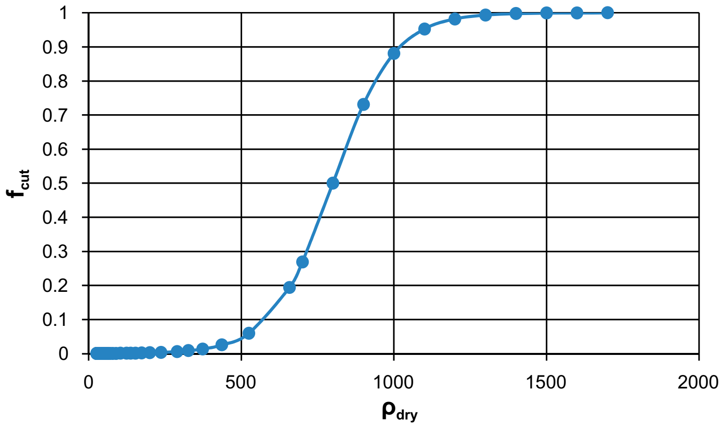

***Figure 2-6.** Cut-off function that gradually decrease the influence of the exponential fit to the high density experimental data. $f_{cut} = 0.5$ at dry density 800 kg/m^3.*

2.3 Shear strength of MX-80 close to CCC

Since the shear strength of MX-80 close to CCC is needed for determining the behaviour of the bentonite at the gel front in a fracture intersecting a deposition hole a number of tests have been done. While there are yield-stress measurements on low-density bentonite systems (Goh et al. 2011) and montmorillonite (Abend and Lagaly 2000, Eriksson and Schatz 2015), no study has been tailored to test the yield strength in the vicinity of the paste-to-gel transition at the CCC.

We have earlier determined the yield stress of homoionic Na-montmorillonite gels extracted from bentonite from Kutch, India (Kutch-Na) by means of rotating- vane rheometry (Hedström et al. 2016). In our experience, Kutch-Na forms gels faster than Wy-Na and Kutch-Na has a lower CCC (~4 mM) than Wy-Na. It is therefore important to test the shear strength of Wy-Na gels, although the erosion tests performed in the past clearly indicate that Wy-Na gels withstand the shearing forces of the flowing water (Hedström et al. 2016). It has previously been found that the formation of gel is relatively insensitive to pH in the range 6–9 (Birgersson et al. 2009, Hedström et al. 2016) and the yield strength is even found to increase at pH above 9 (Goh et al. 2011). Therefore, no attempt to control the pH in the rheological tests presented here has been done.

The state diagram for Wy-Na (Figure 2-1) shows that the gel at the CCC (20 mM) may have as high clay concentration as 60 g/l, while samples prepared at a clay concentration of 80 g/l were pastes, i.e., showed swelling. Thus, the rheology of Wy-Na was tested at [NaCl] = 20 mM for samples with clay concentration around the maximum gel concentration; 50 g/l (below), 60 g/l and 70 g/l (possibly above maximum and thus represent a paste).

The shear stress vs time (strain) behaviour of the Wy-Na samples at high water content was determined by means of rotating-vane rheometry, using a four-bladed vane-spindle (V-74). All tests are performed at a rotational speed of 0.05 rpm. Initially we tested the salt-free systems and the results are shown in Figure 2-7. At clay concentration of 70 g/l the yield stress exceeded the maximum value of the instrument (Brookfield DV II + Pro LV) and the measurement was terminated. Thus maximum measured shear stresses were > 114 Pa (70 g/l), 59 Pa (60 g/l), and 41 Pa (50 g/l). The maximum shear stress will herein be defined as the yield stress. For the sample with clay concentration 50 g/l two tests were conducted. First the sample had been at rest for 4 days and after the measurement the sample was vigorously shaken and left to rest for 2 h. As can be seen in Figure 2-7 the two stress-vs-time curves are almost identical. This suggests that the system finds its equilibrium structure within 2 h and further ageing has minor influence on its rheology. This is in contrast to the gels (see e.g. Table 2-1), where ageing has a pronounced effect on the build-up of a percolated edge-face network.

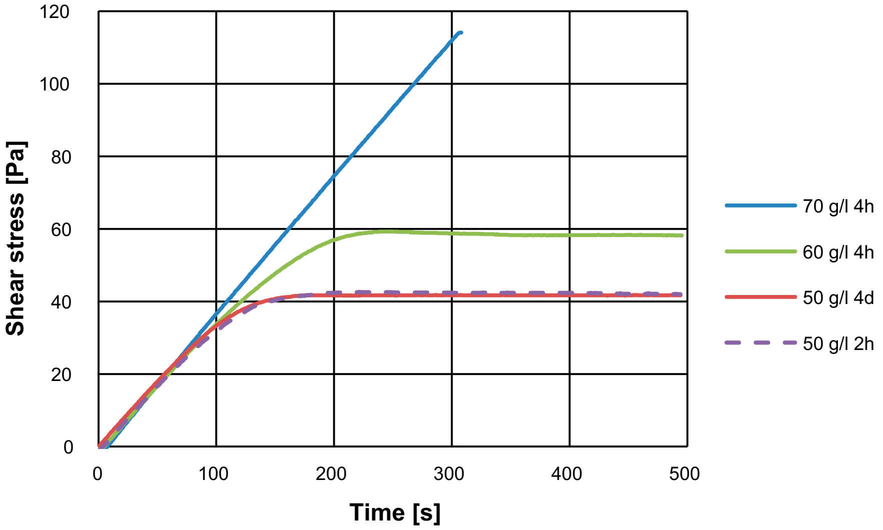

Figure 2-7. Shear stress vs shearing time of Wy-Na under salt free conditions. The rest time after agitation was 4 hours for the 60 and 70 g/l samples and for the 50 g/l sample it was 4 days, and then a repeated test with 2 hours rest time after vigorous agitation was performed.

Note that the salt-free systems do not represent gels since these pastes would swell in contact with water. Thus the shear-stress response in Figure 2-7 reflects the repulsive forces between clay layers because attractive forces are negligible (van der Waals) or absent as the spillover of negative potential effectively inhibit edge-face interactions below the CCC (Hedström et al. 2016, Secor and Radke 1985).

To examine the rheological behaviour of Wy-Na at the CCC, NaCl was added to the three pastes in Figure 2-7; 1 ml of NaCl solution (0.5 M or 0.6 M depending on sample volume so that the final concentration became 20 mM). After addition of NaCl, the clay samples were vigorously shaken and left to rest. After 1 h of rest time shear stress was measured. For all clay concentrations the yield stress had decreased as shown in Figure 2-8. Yield stresses were 5.3, 16.5, and 53.5 Pa for clay concentrations 50, 60, and 70 g/l, respectively. The presence of NaCl reduces the repulsion and that is reflected in the reduction of both yield stress and slope $d\sigma/dt$. Note that the 70 g/l sample is less influenced than the other two, suggesting that it retains some paste character.

The tests were repeated using the same samples: After vigorous shaking the samples were left to rest for 18 h before measuring the shear stress. The results are shown in Figure 2-9. Yield stresses were doubled compared to the values after 1 h rest time in the case of the two lowest clay concentrations, while a factor of 1.5 higher for the 70 g/l sample.

Following the same procedure, the rheology tests were repeated after 44 h rest time. For the 70 g/l sample the changes were only minor as can be seen in Figure 2-10. The yield stress showed some increase for both the 50 and the 60 g/l samples. At 50 g/l the yield stress was 15.3 Pa and at 60 g/l the value was 39.9 Pa. Table 2-1 summarizes the results from Figures 2-8 to 2-10.

The time-dependence on the stress-time curve that is particularly pronounced for the 50 and 60 g/l samples reflects the time for building up an edge-face network. Thus the measured yield strength in these system is foremost related to the strength of the edge-face network (Hedström et al. 2016).

Table 2-1. Maximum yield stress at 20 mM NaCl after different rest times for the three Wy-Na samples.

C_{Clay} [g/l]	σ_{max} [Pa] (after different rest times)		
	1 h	**18 h**	**44 h**
50	5.3	11.5	15.3
60	16.5	33.6	39.8
70	53.5	79.4	81.3

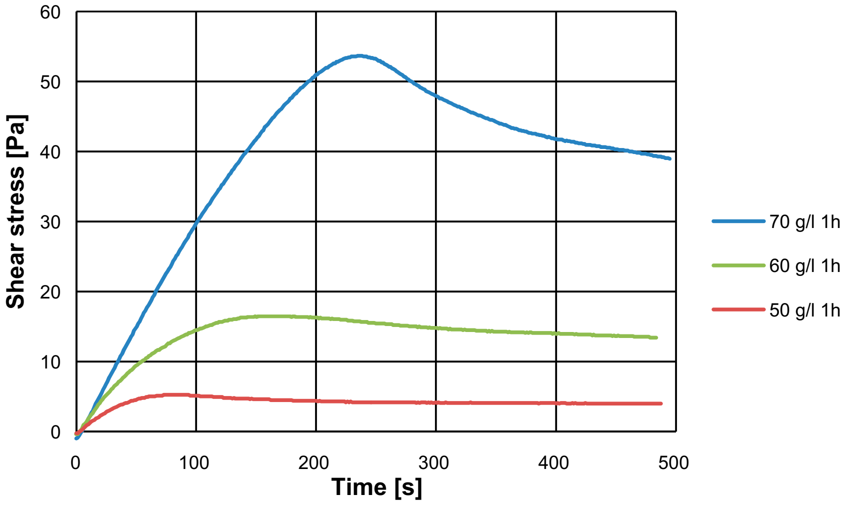

Figure 2-8. *Shear stress vs shearing time of Wy-Na with 20 mM excess NaCl concentration. The rest time after salt addition and agitation was 1 hour for all three samples.*

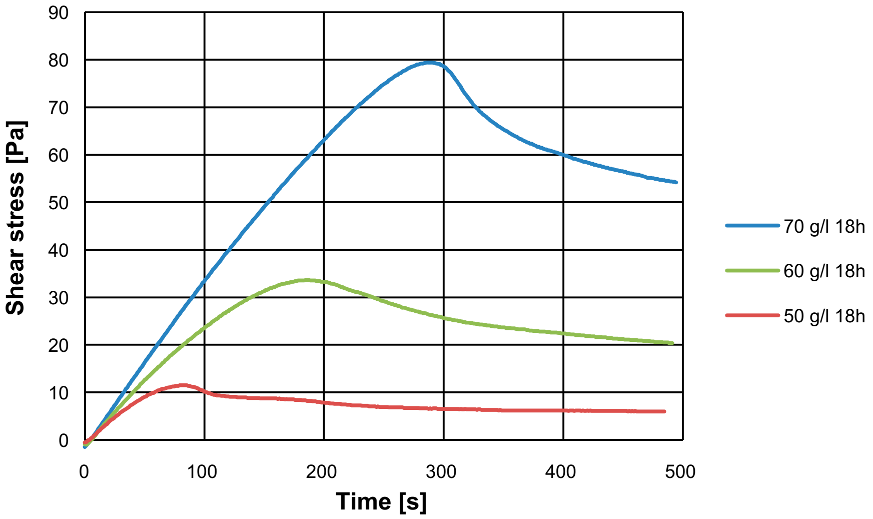

__Figure 2-9.__ Shear stress vs shearing time of Wy-Na with 20 mM excess NaCl concentration. The rest time after vigorous agitation was 18 hours for all samples.

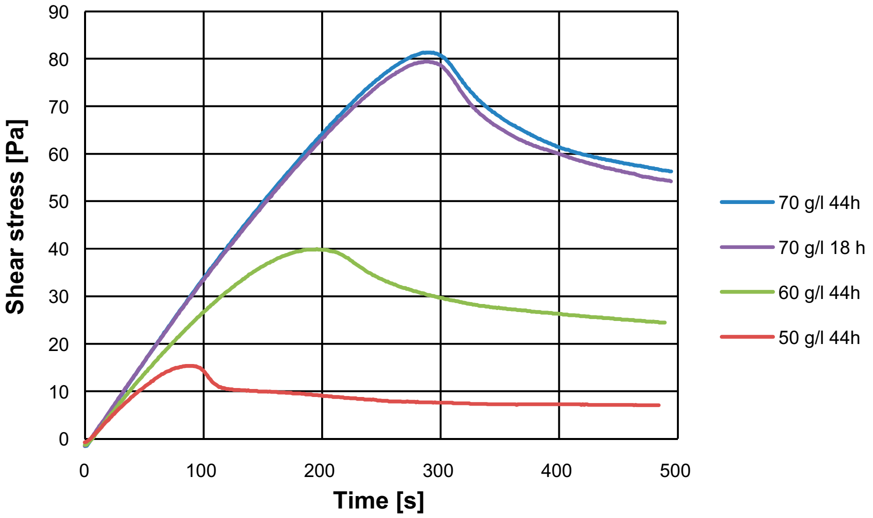

__Figure 2-10.__ Shear stress vs shearing time of Wy-Na with 20 mM excess NaCl concentration. The rest time after vigorous agitation was 44 h for all samples. For comparison the results after 18 h rest time are also shown for the 70 g/l sample.

3 Hydromechanical models of swelling bentonite

3.1 General

In this chapter some models of the hydro-mechanical properties of bentonite are described. These models are based on laboratory measurements extrapolated to very low densities in combination with some theoretical models. They are needed for modelling the bentonite penetration into fractures.

In the performed study, maximum swelling is assumed to be 60 g/L, i.e. at this clay concentration swelling has ceased, and the bentonite does not swell to lower concentrations. Above 60 g/L, swelling is described using hydro-mechanical models described below.

The models only considers completely water saturated conditions, which means that no gas phase is present in the clay. The model for swelling clays is based on the following three basic concepts:

1. The effective stress theory.
2. Swelling pressure and swelling properties.
3. Shear resistance in a clay that counteracts sliding against a surface and change of shape (shear stain).

Since the theoretical knowledge of the basic laws (thermodynamics etc.) that drive these processes is judged to be insufficient, no geochemical or thermodynamic derivations have been done. The models that will be used here for describing the fracture penetration are designed with test results as bases and are thus empirical. This is in agreement with most relationships derived for design purposes in soil mechanics and rheology sciences and also with the modelling performed for SR-Site (Åkesson et al. 2010) and the homogenisation task in phase 2 of the TF EBS.

Large efforts have been made in order to understand and model the swelling and homogenisation processes in bentonite. Examples of laboratory investigations and results are presented in Dueck et al. (2015). Examples of models and modelling results are presented in Börgesson et al. (1995) and Åkesson et al. (2010). The models have been used for finite element modelling of different swelling scenarios, both in order to compare with laboratory tests and in order to understand the function in the actual repository.

No finite element calculations has been performed in this work. Instead a model based on force equilibrium for estimating the penetration into a fracture will be used. In order to be able to use the model two relations are needed:

- The relation between swelling pressure and density.
- The friction angle and the dependency on the normal stress.

In this chapter the models used for these relations will be presented.

3.2 The effective stress theory

The effective stress theory says that the swelling pressure and the pore water pressure are mathematically independent quantities and give a total pressure that is the sum of the pressures:

$$\sigma_t = \sigma + \mathrm{A}u \qquad \text{(Equation 3-1)}$$

where

σ_t = total stress

σ = effective stress = swelling pressure

u = pore water pressure

$\mathrm{A} \approx 1.0$

This theory, which is developed for non-swelling clays has been proven to be valid with a value of A close to 1 for bentonite at pore water pressure lower or similar to the water pressure at repository depth. See e.g. Graham et al. (1992) and Harrington and Birchall (2007).

The water pressure will thus only affect the total stress and not the swelling pressure (except at very high water pressures), which means that the water pressure does not affect the behaviour of the bentonite.

3.3 Swelling pressure and swelling properties

Swelling pressure is a consequence of repulsive forces between clay particles. These forces decrease with distance between the particles. The swelling pressure is thus a function of the density and this relation has been measured in many laboratory studies.

Relation between swelling pressure and density

The relation between swelling pressure and density has been measured in many test series (Börgesson et al. 1988, 1995, Karnland et al. 2006). For the finite element calculations a logarithmic relation between the change in void ratio caused by a change in effective average stress (called Porous Elastic) has been used and verified.

Porous Elastic implies a logarithmic relation between the void ratio e and the average effective stress p according to Equation 3-2 and illustrated in Figure 3-1.

$$\Delta e = -\kappa \cdot \Delta \ln p \qquad \text{(Equation 3-2)}$$

where κ = porous bulk modulus

Poisson's ratio ν is also required. The following values have been derived and validated (Börgesson et al. 1995) for high densities:

$\kappa = 0.21$

$\nu = 0.4$

Equation 3-2 with the given parameter values is not valid for low densities (see Börgesson et al. 1995) but only in the interval $0.7 < e < 1.5$, which correspond to 1 110 kg/m^3 < ρ_d < 1 635 kg/m^3. At lower densities the porous bulk modulus is much larger ($\kappa \approx 1.37$) but this change in modulus is not included in the model and the value is not well known for very low densities. If swelling causes a lower density the swelling will not be correctly modelled for that part.

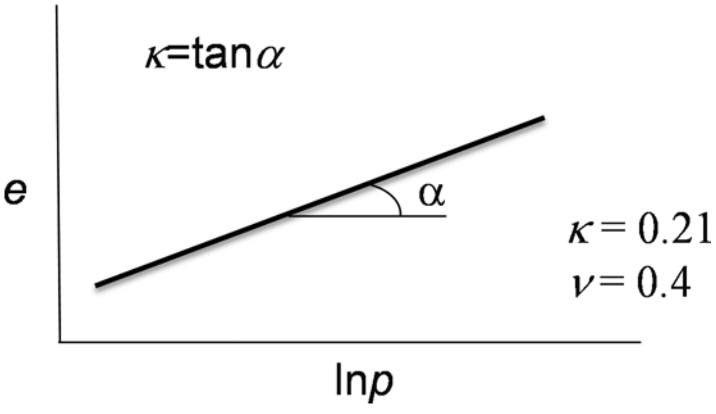

Figure 3-1. *Illustration of Porous Elastic.*

Since the swelling into a fracture yields much lower densities (higher void ratios) a relation different from Equation 3-2 is needed. The semi-empirical relation, Equation 2–1, derived in Chapter 2 and shown as the green line in Figure 2-4 can be used. For convenience we repeat Equation 2–1 here:

$$\sigma_s(\rho_d) = 0.0094 \cdot \exp(0.0086 \cdot \rho_d) + 3 \cdot 10^{-5} \cdot \rho_d^{2.5656} \qquad \text{(Equation 3-3)}$$

where

σ_s = swelling pressure (kPa)

ρ_d = dry density (kg/m^3)

At the paste/gel transition of interest here (ρ_d = 60 kg/m^3), the swelling pressure will according to this relation be 1.1 kPa. Swelling pressure will be assumed to be described by Equation 3-2 down to ρ_d = 60 kg/m^3 and then to take the value 0. We thus get the following expression for the swelling pressure:

$\rho_d \geq 60$ kg/m^3: $\sigma_s = 0.0094 \cdot \exp(0.0086 \cdot \rho_d) + 3 \cdot 10^{-5} \cdot \rho_d{}^{2.5656}$

$\rho_d < 60$ kg/m^3: $\sigma_s = 0$ kPa

However, this is an extrapolation of an expression valid for non-saline solutions and thus may be slightly too high at the CCC and 60 kg/m^3. The discrepancy between DLVO theory and experiment shown in Figure 2-2 coupled with the lack of data above 10 mM NaCl for the low density systems introduce large relative uncertainties regarding the exact swelling pressures. The impact of this uncertainty is analysed in Section 4.3.

3.4 Shear resistance

3.4.1 General

The shear resistance at failure is a function of the effective stress (or swelling pressure) and can be expressed with a friction angle as described by Equation 3-4 and shown in Figure 3-2.

$$\tau_f = \sigma_n \cdot \tan\phi \qquad \text{(Equation 3-4)}$$

where

τ_f = shear stress at failure (kPa)

σ_n = normal effective stress (kPa)

ϕ = friction angle (°)

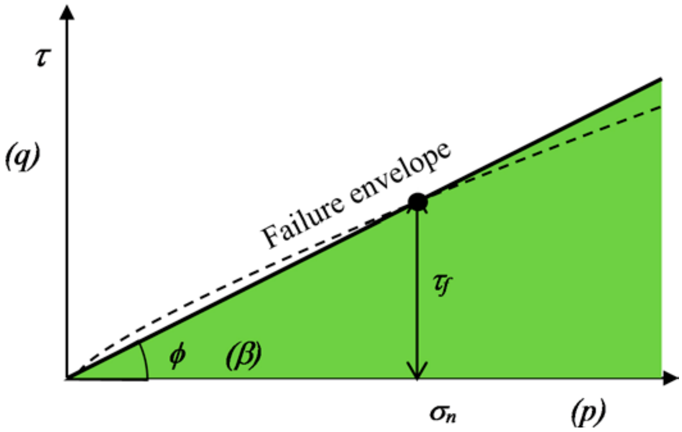

Figure 3-2. *Illustration of the friction angle ϕ derived from the shear strength τ_f valid at the normal stress σ_n. The hatched line is the actual failure envelop. The solid line is the approximation of the failure line to a straight line that can be used for evaluation of the friction angle. β is the "friction angle" in a p-q diagram as described below. The green field illustrates possible stress combinations without failure.*

The clay can sustain shear stresses up to the failure envelope. At the failure envelope the clay will fail and plasticize. The failure envelope may be curved and thus the friction angle will depend on the normal stress.

The friction angle ϕ can be evaluated directly from the τ_f–σ_n relation. If q_f and p are used where

q_f = deviator stress at failure

p = average effective stress

the friction angle can be evaluated from the angle β in the p-q diagram according to Equation 3-5.

$$\phi = \sin^{-1}\left(\frac{3q_f}{q_f + 6p}\right) \qquad \text{(Equation 3-5)}$$

3.4.2 Material models

The result of high shear stresses that approach the failure envelope is non-recoverable deformations, which can be modelled as plastic strains. There are several models for the plastic behaviour of clay. Two models have been used when modelling bentonite swelling with the finite element code Abaqus, namely Drucker-Prager Plasticity model and Claytech Plastic Cap model. These models are described in e.g. Börgesson et al. (1995) and Börgesson et al. (2018).

3.4.3 Friction angle and the dependency on the normal stress

The friction angle of different bentonites has been determined by a number of laboratory tests series mainly performed as triaxial tests (Börgesson et al. 1995, Dueck et al. 2010). Figure 3-3 shows examples of triaxial test results.

Figure 3-4 shows example of evaluated friction angles between bentonite (MX-80) and a surface at different conditions.

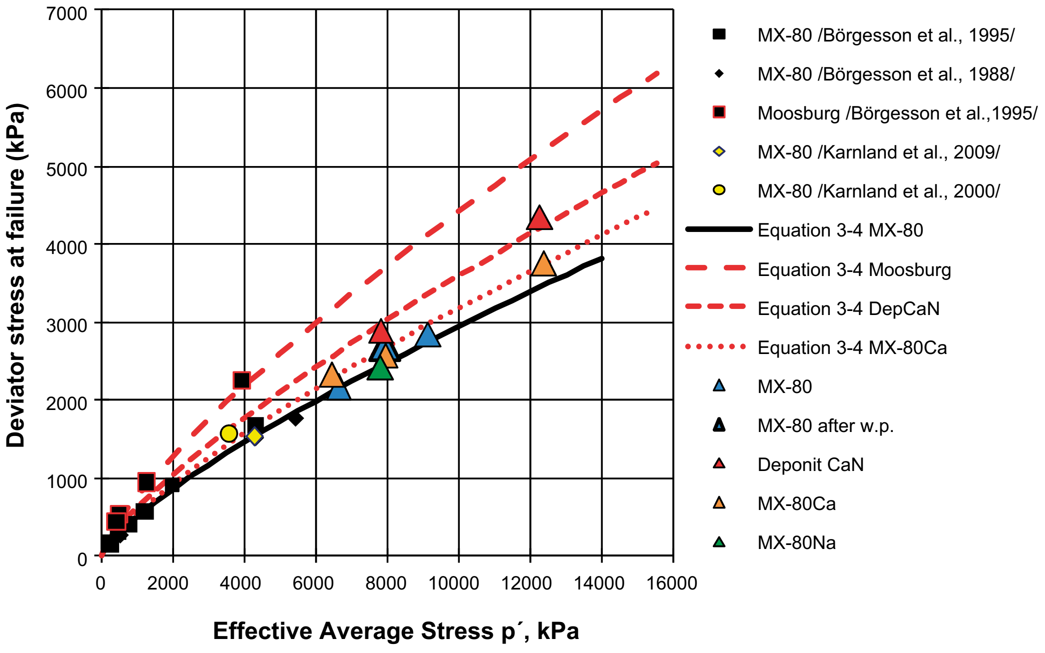

Figure 3-3. Results from triaxial tests with the deviator stress at failure plotted as a function of the average effective stress. The red triangles refer to Deponit CaN, the orange triangles refer to MX-80Ca (MX-80 ion exchanged to Ca), the blue triangles refer to MX-80, and the green triangle represents the test on MX-80Na. The lines represent equations used for modelling (Dueck et al. 2010).

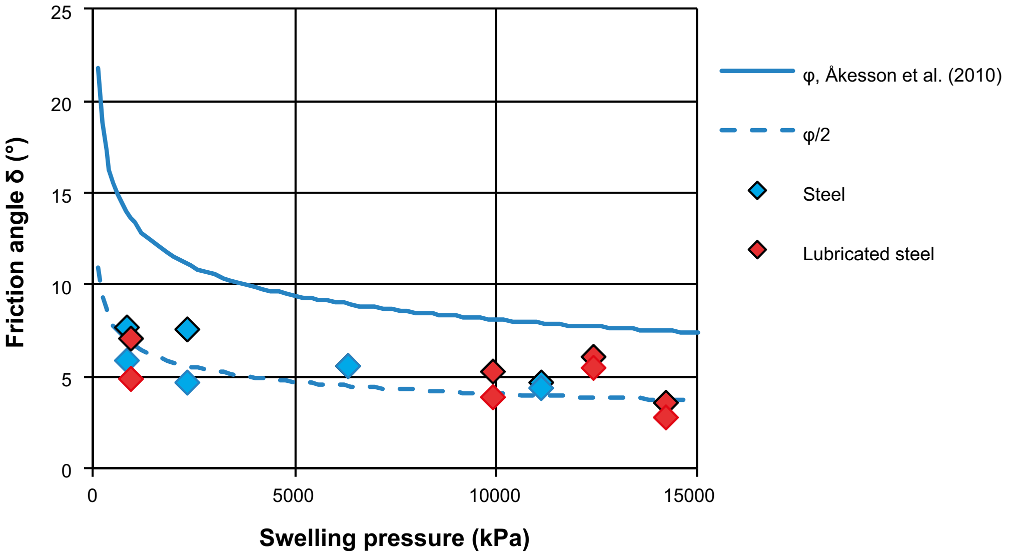

Figure 3-4. *The friction angle between bentonite and a steel surface evaluated from friction tests (Dueck et al. 2015).*

Figure 3-4 shows the results from tests that measure the shear resistance at failure between the bentonite and a plane surface. This resistance differs from the shear resistance in the bentonite itself that can be measured by triaxial tests. This internal friction angle corresponding to the peak strength in the bentonite MX-80 has been evaluated from a number of triaxial tests. These results follow the blue line in Figure 3-4 (Åkesson et al. 2010) derived from the results on MX-80 shown in Figure 3-3, which correspond to Equations 3-5 and 3-6.

$$q_f = q_{f0} \cdot \left(\frac{\sigma}{\sigma_0} \right)^b \qquad \text{(Equation 3-6)}$$

where

q_f = deviator stress at failure

σ = swelling pressure (corresponding to p in Figure 3-3)

q_{f0} = 500 kPa σ_0 = 1 000 kPa and b = 0.77

The results shown in Figure 3-4 indicate that this shear resistance is lower than the peak value of the shear strength. The hatched blue line in Figure 3-4 is drawn as half the friction angle according to the solid blue line, which has been used in modelling exercises. The friction angle increases with decreasing swelling pressure but the basis at low swelling pressure is not very good, due to measuring problems. At the limit above the CCC at the NaCl concentration 20 mM, where the paste stops swelling and becomes a non-swelling gel where the dry density is ρ_d = 60 kg/m^3 and the swelling pressure according to Equation 3-3 is 1.1 kPa the friction angle will according to Equations 3-5 and 3-6 be

Equation 3-6: q_f = 2.64 kPa

Equation 3-5: ϕ = 59°

Using half the peak value for the friction between the bentonite and a metal surface would thus yield ϕ = 30°. However, Equation 3-6 is an extrapolation of measured values, so the result is very uncertain.

The friction angle can also be evaluated from the shear strength measured on low density bentonite in non-saline solutions with vane tests. Figure 3-5 shows a compilation of results taken from Birgersson et al. (2009).

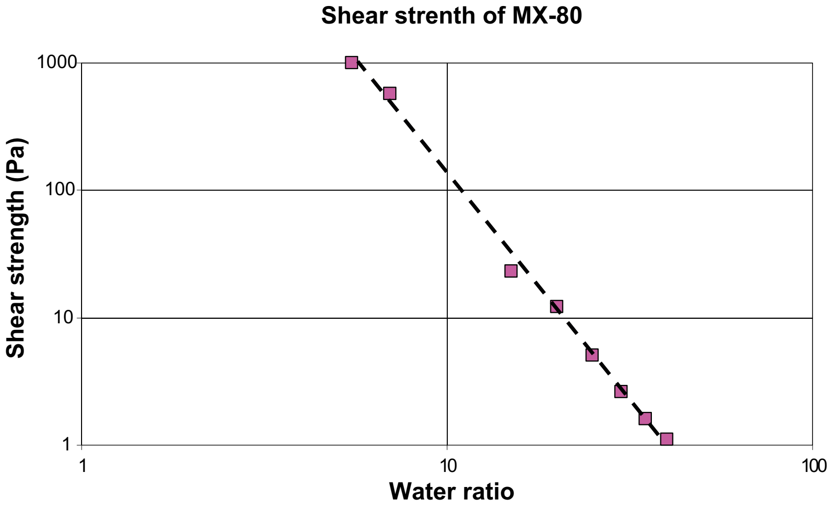

Figure 3-5. *Measured shear strength of MX-80 in distilled water as a function of water ratio after 1 day of rest.*

The shear strength at $\rho_d = 60$ kg/m^3 corresponding to the water ratio $w = 16.7$ will thus according to Figure 3-5 be about 20 Pa. The tests measure τ_f according to Figure 3-2. Using the swelling pressure 1.1 kPa according to Equation 3-3 yields a friction angle of $\phi = 1.04°$ according to Equation 3-4, which is far from the result of using the relation in (Åkesson et al. 2010).

Using the same swelling pressure (1.1 kPa) and the measured values for Wy-Na and non-saline solutions according to Section 2.3 where the shear strength 60 Pa was measured at $\rho_d = 60$ kg/m^3 gives the friction angle $\phi = 3.1°$.

4 Swelling into a plane fracture

4.1 Introduction

In this chapter a model of the penetration of a swelling clay into a plane fracture is described and then used to make a sensitivity analysis of the penetration depth at different possible variations of the two parameters included in the model. The results are compared to some measurement. In addition the influence of gravity in inclined fractures is studied.

4.2 Theory

At first the force equilibrium state that will prevail in a fracture after completed swelling into a plane fracture is investigated and a formula for the swelling pressure distribution in the fracture derived without considering the stress path up to the equilibrium state.

The bentonite swelling into an ideal plane fracture can be modelled as controlled by the swelling pressure of the bentonite and the friction against the fracture wall. The actual swelling will not be considered but only the situation after completed swelling and pore pressure equalization.

Figure 4-1 shows the equilibrium situation of an infinitesimal part of a bentonite (*dr*) penetrating from a deposition hole into a horizontal fracture.

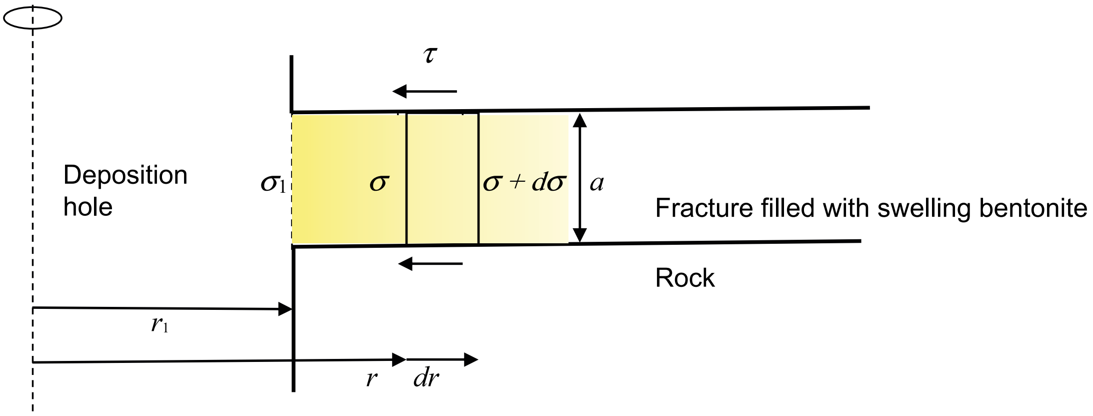

***Figure 4-1.** State of equilibrium of an infinitesimal part of bentonite dr after swelling into a fracture where*

r_1 = *deposition hole radius*

a = *fracture aperture*

σ_1 = *swelling pressure at the deposition hole wall*

σ = *swelling pressure at the distance* $r-r_1$ *into the fracture*

$d\sigma$ = *change in swelling pressure at the increased distance dr*

τ = *shear stress at the fracture wall*

The shear stress between the penetrating bentonite and the fracture wall can be expressed as

$\tau = \sigma \tan \phi$

where

ϕ = friction angle between the bentonite and the fracture surface

Force equilibrium in radial direction yields according to Appendix 1:

$$\ln\sigma(r) = \ln\sigma_1 + \ln\frac{r}{r_1} - \frac{r-r_1}{a}\cdot 2\tan\phi \tag{Equation 4-1}$$

Applying the penetration depth $z = r - r_1$ and assuming that the penetration depth is small compared to the radius r_1 ($r/r_1 \approx 1$) yields

$$\ln\sigma(z) = \ln\sigma_1 - \frac{z}{a}\cdot 2\tan\phi \tag{Equation 4-2}$$

or

$$\sigma = \sigma_1 \cdot e^{-2\tan\phi\left(\frac{z}{a}\right)} \tag{Equation 4-3}$$

Equation 4-3 thus describes the relation between the swelling pressure σ in the fracture and the penetration depth z into the fracture at the fracture aperture a and the buffer swelling pressure σ_1 if the influence of axial symmetry is neglected (can be done since the radius of the deposition hole is large compared to the penetration depth). Equation 4-3 only describes the equilibrium state and does not consider the stress path or stress history.

4.3 Calculated fracture penetration

Figure 4-2 shows the swelling pressure distribution in a plane fracture with the aperture 0.1 mm at different friction angles calculated according to Equation 4-3.

Figure 4-2 shows that the swelling pressure drops rapidly. At the friction angle 10° it drops from 7 MPa at the deposition hole to below 10 Pa at 4 mm depth of a 0.1 mm wide fracture.

A problem is the insufficient knowledge of the swelling pressure and friction angle at the very low densities down to 60 kg/m^3 where swelling stops when the ground water has a salinity above the CCC. As shown above different ways of evaluating these parameters yield very different results. However, it could be useful to make a sensitivity analysis in order to study how much the penetration can vary.

The swelling pressure is modelled to drop instantly from a value estimated at the clay concentration 60 g/L as shown in Section 2.1 to zero at lower clay concentrations and the calculation refers to the penetration depth at the estimated swelling pressure just before the drop.

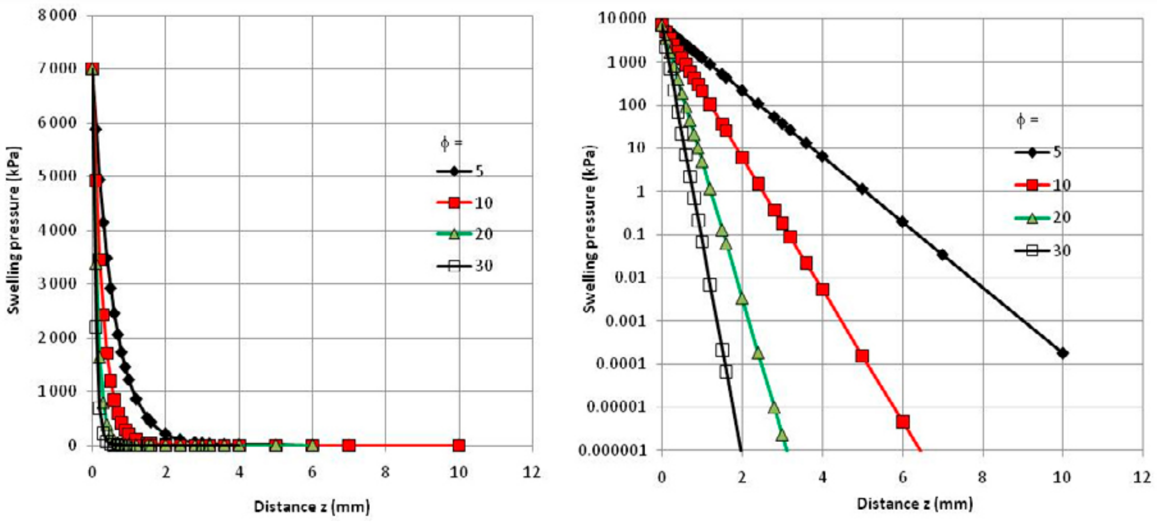

Figure 4-2. *Calculated swelling pressure as a function of depth after penetration of bentonite into a plane fracture with the aperture 0.1 mm at different friction angles.*

The penetration depth can be calculated with Equation 4-4 (derived from Equation 4-2).

$$z = \frac{a}{2\tan\phi}\ln\frac{\sigma_1}{\sigma} \qquad \text{(Equation 4-4)}$$

Varying ϕ between the extreme values $0.5° < \phi < 30°$ and σ between the extreme values 0.01 kPa $< \sigma <$ 1.1 kPa we can get the penetration depths shown in Table 4-1. The fracture width is in this case a = 100 µm and the swelling pressure of the buffer at the fracture entrance σ_1 = 7 000 kPa.

Table 4-1. Calculated fracture penetration depths at different friction angles and swelling pressure limits σ.

	ϕ =0.5°	**ϕ =1.0°**	**ϕ =5°**	**ϕ =10°**	**ϕ =30°**
σ = 0.01 kPa	z = 77 mm	z = 39 mm	z = 7.7 mm	z = 3.8 mm	z = 1.2 mm
σ = 0.1 kPa	z = 64 mm	z = 32 mm	z = 6.4 mm	z = 3.2 mm	z = 0.97 mm
σ = 1.1 kPa	z = 50 mm	z = 25 mm	z = 5.0 mm	z = 2.5 mm	z = 0.76 mm

Table 4-1 shows that the penetration depth varies up to a factor 100 at the extreme cases of friction angles 0.5 and 30 degrees and swelling pressure 0.01 and 1.1 kPa at the dry density $\rho_d = 60$ kg/m^3 but is anyway not larger than 77 mm at the most extreme case.

The uncertainties of these calculations are beside the friction angle and the swelling pressure mainly the validity of Equation 4-3 and the simplification done that we have a fracture with the same properties as parallel plates. The derivation of Equation 4-3 is based on force equilibrium after completed swelling and does not take into account the swelling phase. The influence of the history of swelling is regarded as small compared to the uncertainties of the swelling pressure and the friction angle and similar expressions for swelling of bentonite have been used in many other calculations. The assumption of parallel plates is judged to increase the penetration compared to if variable fracture apertures were considered.

4.4 Comparison with measurements

One fracture test with free swelling in an artificial fracture with the aperture a = 120 mm in a water with the salinity 25 mM, i.e. above the CCC has been performed (Hedström et al. 2016). Figure 4-3 shows the result. When setting up this experiment, the water-saturated clay at the source (annular cylinder) was to a small extent mechanically extruded into the fracture when the fracture was closed, thus the clay in the fracture has the same density as in the source. This point constitutes the starting point for swelling, and has been outlined with a red circle in Figure 4-3. During the initial 48 h, some swelling (1–2 mm) is evident. Despite this, after the initial two days no more swelling was experienced and the clay appears to have formed a stable gel at the edges, which does not release sol particles into the fracture. The solution was left stagnant in the fracture for 10 days. After this time, the solution was flowed through the fracture at various velocities. During the flow phase, the NaCl concentration was also gradually lowered in steps of 5 mM. Neither erosion, nor expansion were observed until day 41 at which point the salinity was changed from 10 to 5 mM. Clearly there is a hysteresis effect involved; once a gel has been formed it remains more or less intact even when the salinity is lowered below the CCC. However, details of the origin of this hysteresis and gel stability below CCC remain largely unknown. Therefore it is still premature to include these effects in modelling. On the other hand, above the CCC, there are no indications that gels would deteriorate over time (Hedström et al. 2016).

The density of the mechanically extruded clay is the same as in the source and has the same characteristics. However, the extrusion from this initial state may be somewhat smaller (some mm) than it would have been if the clay had not been mechanically extruded, since the supply of clay in the latter case would have been higher. Note that the purpose of the experiment in Figure 4-3 was primarily to investigate erosion above the CCC and not to determine if the exact extent of extrusion would be 1–2 mm or 2–3 mm.

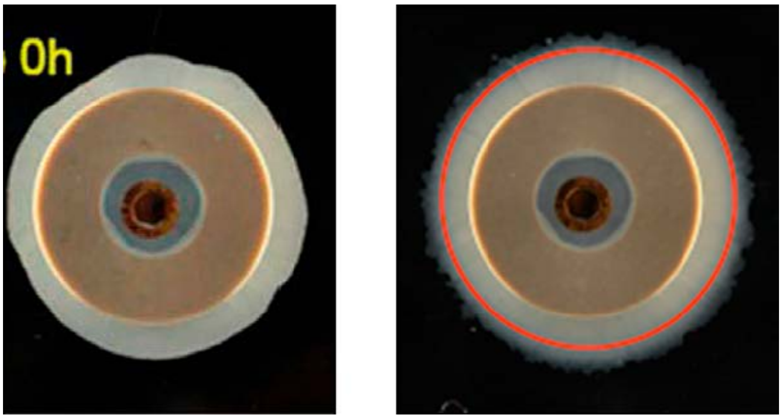

Figure 4-3. *Top view of a 1 cm thick Na-montmorillonite annular cylinder that swells into a 120 µm fracture. The outer diameter of the annular cylinder (darker grey) is 35 mm. The initial extrusion of clay gel (left picture) is mechanical and happened when the fracture top was mounted and thus not caused by swelling. The fracture is filled with 25 mM NaCl solution adjusted to pH > 9. After 24 h swelling was completed and a gel formed at the outer rim of the clay (right picture) that prevents further expansion. For 10 days the solution was left stagnant. The right figure shows the swelling from the initial state marked with a red line.*

Below the CCC there are several swelling tests reported from our laboratory (Hedström et al. 2016). In DI water as well as in Grimsel water simulant the clay paste swells about 10 to 15 mm into a 120 µm fracture. Outside this paste a sol is observed and in stagnant water the amount of sol increases slowly with time, while in slowly seeping water the sol is transported away. The paste however, is unaffected by the flow which is in line with its measured shear strength reported in Figure 2-7 and by e.g., Eriksson and Schatz (2015). The average clay content of the sol accumulated outside the paste rim was estimated to be about 30 g/l (Hedström et al. 2016).

In our setup we have taken measures to prevent deformation and bulging of the fracture. If that is overlooked, larger extrusions might be possible, but such results are artefacts and not relevant for the actual repository. In the literature we have found two studies where we are confident that the fracture aperture has been well controlled. Baik et al. (2007) studied extrusion and erosion of a Korean Ca-bentonite "Gyeongju bentonite" using an artificial fracture setup made from granite and a bentonite dry density at the source of 1 440 kg/m^3. Gyeongju bentonite has a cation exchange capacity of 0.71 eq/kg and a montmorillonite content of 70 wt%. Since this bentonite is dominated by calcium one does not expect extensive swelling and the tests showed only a 3 mm extrusion into the 0.5 mm-aperture fracture. The bentonite source in this test was large in comparison to the amount of extruded bentonite.

In another study on Rokle bentonite, which also is dominated by divalent cations (Ca and Mg) it was found that the bentonite extrusion was about 4 times the aperture (Svoboda 2013) for the tested apertures of 5, 10 and 15 mm. With such large aperture there is of course a concern that the dry density of the source is substantially lowered as the clay is swelling into the fissure. However, the initial dry density was as high as 1 600 kg/m^3 and at the 5 mm aperture the volume of the clay filling the fracture only amount to 4% of the source volume.

As Na-montmorillonite contacted with saline solution above the CCC shows limited swelling it may be justified to compare our extrusion results with the work of Baik et al. as well as Svoboda and conclude that the extrusion limited to a few mm is corroborated.

The same calculation of the bentonite penetration as was presented in Table 4-1 was performed for the test shown in Figure 4-3 and the results are given in Table 4-2. The fracture width is in this case a = 120 µm and the swelling pressure of the buffer at the fracture entrance σ_l = 3 084 kPa derived from the density at saturation 1800 kg/m^3 or the dry density ρ_d = 1250 kg/m^3 according to Equation 3-2.

Table 4-2. Calculated fracture penetration depths *z* at different friction angles and swelling pressure limits σ.

	$\phi = 0.5°$	$\phi = 1.0°$	$\phi = 5°$	$\phi = 10°$	$\phi = 30°$
$\sigma = 0.01$ kPa	$z = 87$ mm	$z = 43$ mm	$z = 8.7$ mm	$z = 4.3$ mm	$z = 1.3$ mm
$\sigma = 0.1$ kPa	$z = 71$ mm	$z = 36$ mm	$z = 7.1$ mm	$z = 3.5$ mm	$z = 1.1$ mm
$\sigma = 1.1$ kPa	$z = 55$ mm	$z = 27$ mm	$z = 5.4$ mm	$z = 2.7$ mm	$z = 0.83$ mm

The very small measured penetration 1–2 mm agrees best with the high friction angle 30 degrees. This speaks for using relations 3-5 and 3-6 for evaluating the friction angle rather than Figure 3-4 and Equation 3-3 since half the values of Equations 3-5 and 3-6 gave the friction angle 30° as evaluated earlier. However, as analysed earlier the measured swelling is probably somewhat underestimated due to the limited access to bentonite in the mechanically extruded clay.

The swelling pressure limit has rather small influence on the penetration depth.

Back-calculating the swelling pressure by using the measured shear strength 20 Pa and the friction angle 30 degrees yields $\sigma = 35$ Pa.

In spite of the large uncertainties regarding swelling pressure and friction angle it is clear that the penetration depth is very small even for extreme values.

4.5 Influence of gravity

Gravity has not been included in the models dealt with in this chapter so the theories are strictly spoken only valid for horizontal fractures. However, the stresses caused by the own weight of the bentonite penetrating a fracture are very low compared to the stresses caused by swelling, friction against the fracture surfaces and the shear strength of the bentonite paste so the influence of gravity is insignificant. This is illustrated by some calculation examples shown in this section.

The worst case of an inclined fracture is a vertical fracture located under the deposition hole. Figure 4-4 illustrates the condition of bentonite penetrating such a fracture.

Figure 4-4 illustrates a situation when a vertical fracture below a deposition hole containing bentonite buffer with the density at saturation $\rho_m = 2\,000$ kg/m^3 is penetrated with bentonite. Ignoring gravity the swelling pressure is reduced along the fracture according to Equation 4-3 until it reaches the dry density $\rho_d = 60$ kg/m^3 where the bentonite stops swelling above CCC.

a = fracture width, $a = 100\ \mu\text{m} = 1.0 \cdot 10^{-4}$ m

l = penetration depth (m)

d = thickness of non-swelling gel (m)

The gravity is acting on two parts of the bentonite. Firstly the gravity acts on the swelling bentonite along the distance l from the deposition hole. The swelling and the gravity is counteracted by the friction against the fracture walls. Secondly the gravity acts on the non-swelling gel with the depth d that may be formed below the depth l. Since there is no swelling pressure there is no friction so the loss of bentonite is only hindered by the strength of the non-swelling gel. We want to know to what extent the gravity may influence the penetration depth.

Since the fracture is water filled we must reduce the effect of the density with the density of water. The dry density $\rho_d = 60$ kg/m^3 corresponds to a density at saturation of $\rho_m = 1\,040$ kg/m^3. The effective density under water is thus $\rho'_m = 40$ kg/m^3. The density at saturation of $\rho_m = 2\,000$ kg/m^3 yields the effective density under water $\rho'_m = 1\,000$ kg/m^3.

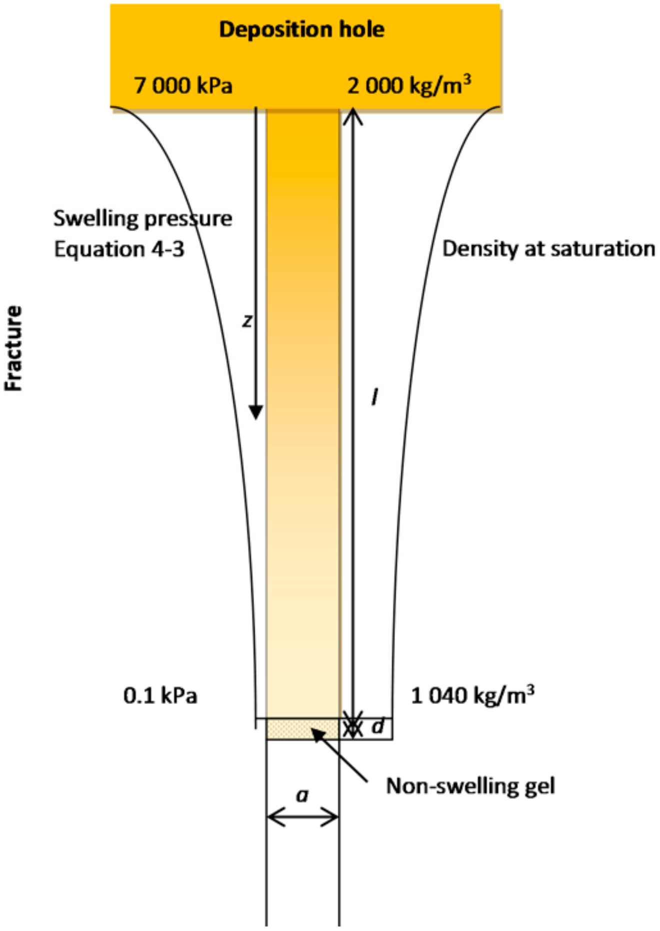
Deposition hole
7 000 kPa
2 000 kg/m³
Swelling pressure
Equation 4-3
Density at saturation
Fracture
z
l
0.1 kPa
1 040 kg/m³
d
Non-swelling gel
a

Figure 4-4. *Illustration of bentonite penetrating a vertical fracture below a deposition hole.*

Gravity acting on the bentonite along the distance *l*

Since the force from the gravity on the bentonite in the fracture is expected to be very small compared to the frictional forces on the fracture surfaces we will only make a very approximate calculation by using the swelling pressure at $z = l/2$ as an average value. In addition we will used the values derived in Section 4.2 and Table 4-1 with the following values of swelling pressure limit and friction angle

$\sigma = 0.1$ kPa

$\phi = 5°$

which yielded the penetration depth into the 100 µm fracture

$l = 6.4$ mm

The swelling pressure at $z = 3.2$ mm will according to Equation 4-3 be

$\sigma = 7\,000 \cdot e^{-2 \cdot (3.2/0.1) \cdot \tan 5°} = 26$ kPa

Using this value as an average yields the following relation at force equilibrium on the entire fracture filling column in addition to the influence of the swelling pressure

$$F = alg\rho'_m = 2l\tau \text{ (kN/m)} \qquad \text{(Equation 4-5)}$$

where

ρ'_m = average effective density under water = (1.0+0.04)/2 = 0.52 kg/dm³

$g = 10$ m²/s

$\tau = \sigma \cdot \tan\phi$ (kPa)

The friction angle that needs to be mobilized in order to prevent displacement of the bentonite column will according to Equation 4-5 be

$\tan\phi = ag\rho'_m/(2\sigma) = 0.0001 \cdot 10 \cdot 0.52/(2 \cdot 26) = 1.0 \cdot 10^{-5}$

$\phi = 0.0006°$

The extra friction angle required is thus negligible compared to the actual average friction angle 5°.

Gravity acting on the bentonite along the distance *d*

Force equilibrium on the gel with the depth *d* yields (per meter fracture width)

$F = adg\rho'_m = a\tau_f$ (kN/m)

where

$\rho'_m = 0.04$ kg/dm^3

$g = 10$ m^2/s

τ_f = strength of the gel (kPa)

According to Section 2.3 the strength of the non-swelling gel at 20 mM excess NaCl concentration at the dry density $\rho_d = 60$ kg/m^3 is 40 Pa 44 after hours rest. This yields the required depth of the gel in order to overcome the strength of the gel:

$d = 0.04/(10 \cdot 0.04) = 0.1$ m

The gel must thus have a depth of 0.1 m in order for the gravity to overcome the strength of the gel. Since the gel is non-swelling it cannot penetrate that deep into the fracture.

The conclusion of these examples is thus as expected that the influence of gravity in a fracture is negligible at NaCl concentrations in the groundwater above CCC.

4.6 Discussion and conclusions

A theory that models the penetration depth of a swelling clay into a fracture has been described and used to make a sensitivity analysis of the penetration depth at different possible variations of the two parameters included in the model. The results for a fracture with the aperture 0.1 mm show that the penetration depth is rather small for the wide range of used values of the friction angle and the limiting swelling pressure (where the gel stops swelling). Varying the friction angle from 0.5° to 30° and the swelling pressure from 0.01 kPa to 1.1 kPa yields a variation in penetration depth from 77 mm (at the lowest friction angle and swelling pressure) to 0.76 mm (at the highest combination), which corresponds to 1–770 times the fracture aperture. This shows that, in spite of the uncertainty in swelling pressure and friction angle, the penetration depth is very limited. The results of measurements in artificial fractures confirm those calculations since at salt contents above CCC the penetration depth is very small compared to the fracture aperture. Even for salt contents below CCC the measured penetration depth of the gel has been limited to about 100 times the fracture aperture.

The gravity that affects the gel in an inclined fracture in a groundwater above CCC has no influence on the penetration depth. Calculations show that even in a vertical fracture the influence of gravity is negligible.

The uncertainty of the model is in addition to the friction angle and the limiting swelling pressure a couple of processes namely creep and hysteresis effects in the bentonite. The creep is small as analysed in Section 5.3. The effect of hysteresis may be important since the model only handles the stress equilibrium after completed swelling so the swelling is not included. However, the influence of hysteresis on the friction angle and the swelling pressure is small compared to the variation of those parameters done in the sensitivity analysis.

5 Proof of existence of shear resistance or friction

5.1 General

In this chapter the existence of shear resistance in a swelling bentonite is proven with examples of long term measurements and creep tests.

As described earlier there is a shear resistance in clay that counteracts sliding against a surface and change of shape (shear stain). This shear resistance can be seen as a friction angle or a density dependent and effective stress dependent shear strength. There are numerous proofs that such a shear resistance exists also in bentonite.

Tests to investigate the shear behaviour of water saturated bentonite have been done and are reported in many reports and articles. For SKB the following tests have been done and are reported (examples):

Triaxial tests at different densities and swelling pressures (Börgesson et al. 1988, 1995, Börgesson 2001, Dueck and Nilsson 2010)

- Homogenisation tests with swelling in different geometries (Dueck et al. 2011, 2014, 2015, Johannesson et al. 2008).
- Friction tests with sliding against different surfaces (Dueck et al. 2011, 2014, 2015).
- Bentonite swelling into thin fractures (Birgersson et al. 2009, Hedström et al. 2016).
- Creep tests (Börgesson et al. 1988, 1995).

Especially interesting are the long tube tests that are running in order to investigate the long term behaviour of bentonite with large density differences in long tubes. Also creep tests illustrating the small creep that takes place in bentonite are interesting.

Additional proof of the existence of remaining frictional stresses in bentonite is the use of porous stones and steel filters in all kinds of bentonite test set-ups. In basically any test involving confined bentonite, the bentonite is in contact with one or several external water solutions through partitioning filters with typical pore sizes in the range 2–50 µm. Under conditions where the external solution is above CCC, the consistent observation is that no bentonite is lost through the filters. Hence, although the filters are typically only a few mm thick, they are able to maintain pressure differences on the order of tenths of MPa. In contrast, under conditions where the external water is below CCC – i.e. under conditions when the bentonite forms a liquid sol rather than a solid gel – bentonite has been demonstrated to easily be eroded through these kind of porous filters. In combination, these observations show that it is the frictional properties of the non-swelling gel which is the ultimate cause for confining the bentonite specimens (while the filter pores are large enough to let through individual montmorillonite particles in a sol phase).

5.2 Homogenisation of bentonite in long tubes

Tests of homogenisation in long tubes are ongoing with the purpose to investigate:

- The ability of bentonite to homogenise in long tunnels or boreholes.
- The influence of friction between bentonite and different surface structures.
- The long term behaviour of large density differences.

Ten tests with low density bentonite pellets in contact with high density compacted bentonite blocks installed in long steel tubes have been started. In most tests, tubes with the diameter 26 mm and the length 250 mm were used. One of the tests (FLR5) has been terminated and sampled for determination of the density distribution. The other tests will be terminated after different times in order to see the influence of time on the homogenisation.

The set-up was designed with the idea that the swelling of the high density bentonite and the compression of the low density bentonite will take place in the central parts of the tube and the difference in swelling pressure will be taken by the friction between the bentonite and the walls of the tube. The length of the tube is designed so that initial densities of the bentonite in the uppermost part of the pellet section and in the lowermost part of the high density section shall remain intact and the density decrease will take place without affecting the end densities.

Figure 5-1 shows the set up and the expected density/swelling-pressure equilibrium after finalized homogenisation. Bentonite with two very different densities are installed in each half of the tube. The initial density at saturation in the lower and upper halves are respectively

ρ_d = 1 534 kg/m^3 (lower half including the slot between the blocks and the grooved tube).

ρ_d = 880–950 kg/m^3 (upper half including the slot between the blocks and the grooved tube).

The density span in the pellets part is related to uncertainties caused by the fact that the pellets are rather big compared to the diameter of the tube.

The measured dry density distribution in test FLR 5 after two years is shown in Figure 5-2.

One test has up to now been running for about 5 years. (FLR2) The measured swelling pressure is shown in Figure 5-3 (Dueck et al. 2017).

Figure 5-2 shows that the transition from the low density to the high takes place along a distance of about 190 mm, which would correspond to length L of the transition zone in Figure 5-2.

Figures 5-2 and 5-3 show that the initial dry densities at the end parts of the tube are unaffected and that the dry density is successively reduced from the high block density to the low pellets density along about 190 mm of the 250 mm long tube due to swelling of the blocks and compression of the pellets. The friction in the bentonite and between the bentonite and the perforated tube surface hinders

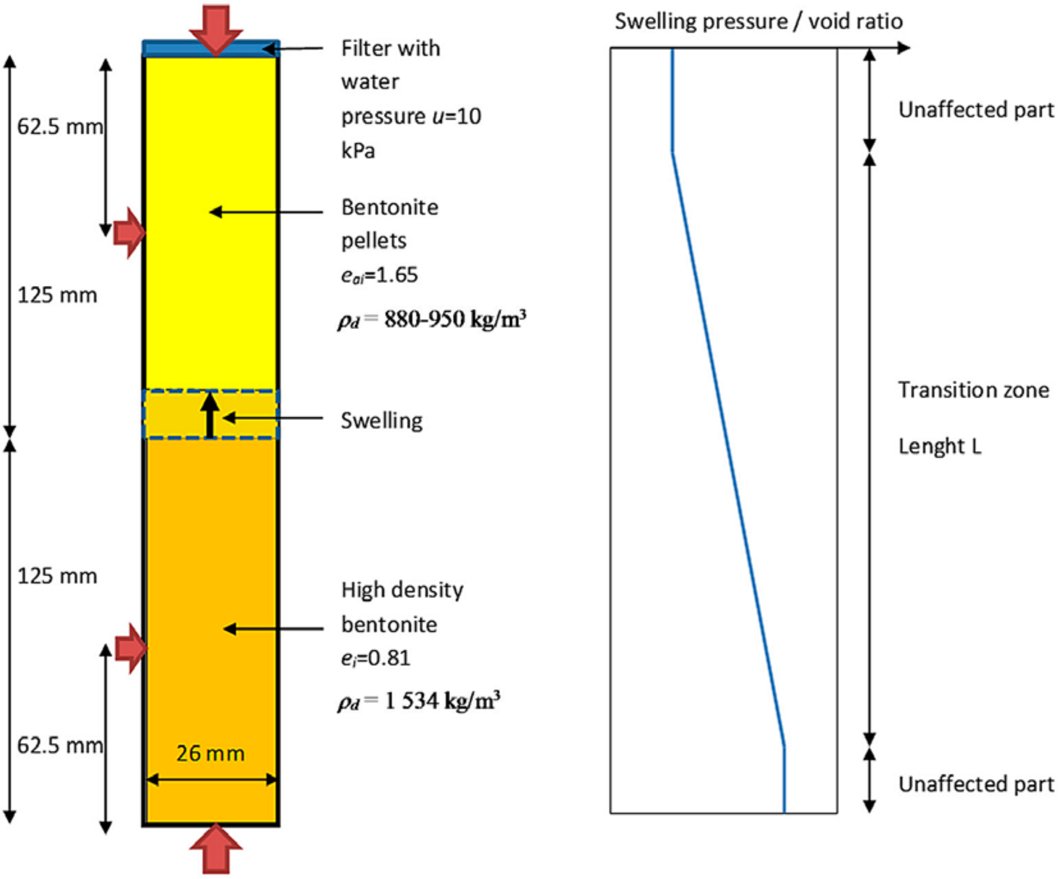
62.5 mm
125 mm
125 mm
62.5 mm
26 mm
Filter with water pressure u=10 kPa
Bentonite pellets
e_{0i}=1.65
ρ_d = 880-950 kg/m^3
Swelling
High density bentonite
e_i=0.81
ρ_d = 1 534 kg/m^3
Swelling pressure / void ratio
Unaffected part
Transition zone
Lenght L
Unaffected part

***Figure 5-1.** Illustration of the test and the expected results. Swelling pressure is measured at four locations (red arrows), two at the high density part and two at the low density part*

the homogenisation. Evaluation of the friction angle based on the measured results in Figure 5-2 and a similar modelling as was done for Equation 4-1, but with the geometry of a tube instead of a slot, yields a friction angle of about $\phi = 7°$ (Dueck et al. 2017).

Figure 5-3 shows that the measured swelling pressures are virtually constant after 2–3 years, which indicate that there is very little or no creep that increases the homogeneity. The remaining 9 tests will be terminated and sampled after different times in order to further study the long term influence.

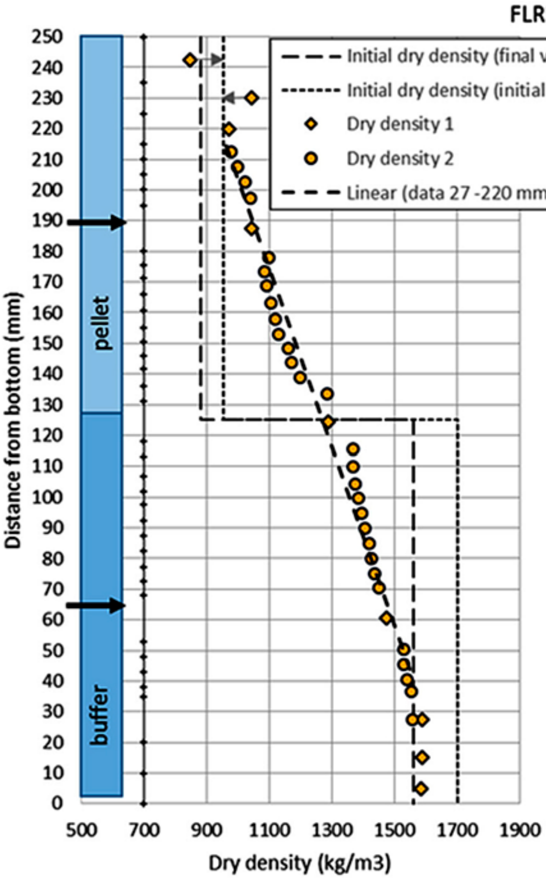

Figure 5-2. *Initial estimated density distribution and measured density distribution at termination after two years test in one of the long tube tests.*

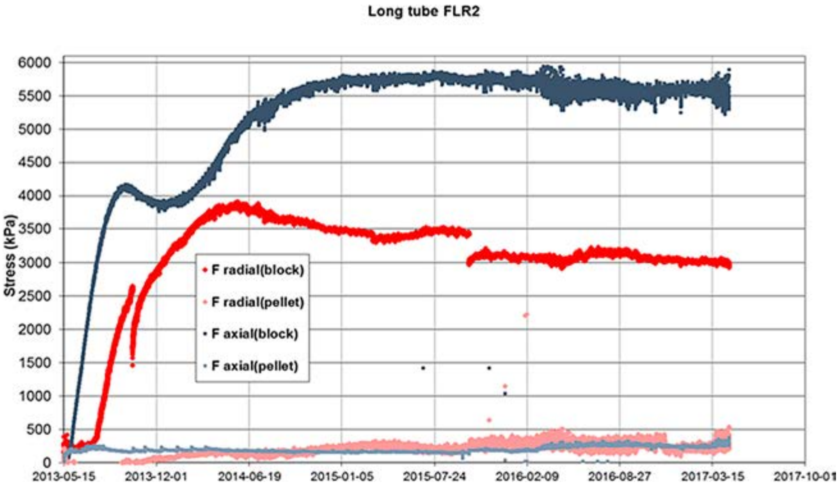

Figure 5-3. *Measured swelling pressure in the long tube test No. 2. The location of the transducers are shown in Figure 5-1.*

5.3 Creep of bentonite measured in triaxial cells

A number of creep tests were performed in the late 1980s with the main purpose to study the possible long term sinking of a canister in a deposition hole. The results and the models derived are reported by Börgesson et al. (1995). The tests were made in triaxial cells where a water saturated bentonite specimen confined in a rubber membrane was at first exposed to an isotropic cell pressure equal to the swelling pressure and then loaded with a constant axial stress yielding a deviator stress that was lower than the failure stress. The relation between the applied deviator stress and the deviator stress at failure is named the degree of mobilised strength D_r.

$$D_r = (\sigma_1 - \sigma_3)/(\sigma_1 - \sigma_3)_f \qquad \text{(Equation 5-1)}$$

where

$(\sigma_1 - \sigma_3)$ = applied deviator stress

$(\sigma_1 - \sigma_3)_f$ = deviator stress at failure

By setting up a number of triaxial creep tests with different degrees of mobilised strengths and measure the axial deformation of the sample with time a creep model could be derived (Börgesson et al. 1988, 1995).

Figure 5-4 shows two examples of creep tests. Altogether 11 creep tests have been performed an all showed similar power-law relations between the strain rate and time; the strain rate decreases with time with the inclination $n = 0.8–1.0$ in the double logarithmic diagram. The creep rate decrease is very fast and already after 10^6 seconds (1.5 weeks) the creep rate is in the order of 10^{-9} 1/s.

Simplifying this example to bentonite creeping in a fracture with the width of $d = 0.1$ mm a creep rate of 10^{-9} 1/s would mean a displacement rate in a fracture of

$dz = 10^{-9} \cdot d/2 = 0.5 \cdot 10^{-12}$ m/s

which corresponds to the rate 0.016 mm in one year after only 1.5 weeks.

Although this is a rather crude example it illustrates that the creep rate is very low and decreases fast to infinitesimal values.

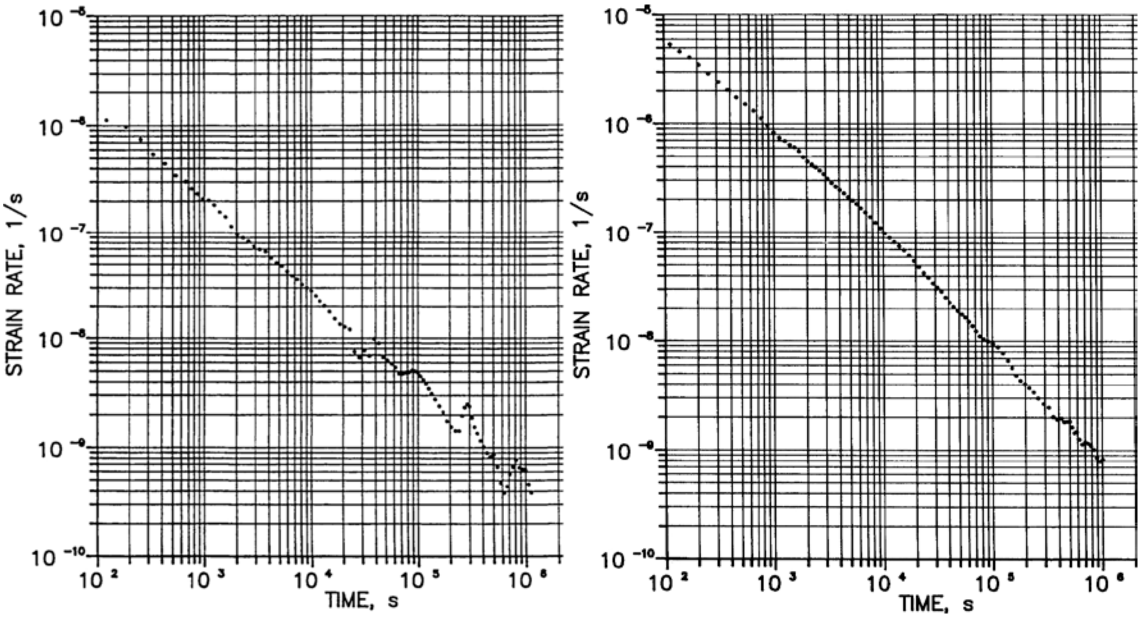

Figure 5-4. *Two examples of creep tests on bentonite. TCR8 to the left with the density at saturation 1 990 kg/m*^{3} *and the degree of mobilised strength 0.4. TCR9 to the right with the density at saturation 2 010 kg/m*^{3} *and the degree of mobilised strength 0.64. (Börgesson et al. 1988, 1995)*

5.4 Conclusions

The existence of frictional forces that counteracts swelling has been shown in numerous tests on bentonite. The friction both acts between the bentonite and the adjacent surfaces and in the bentonite as resistance to changes in shape (shear strain). Long term tests in long tubes show that these forces do not change significantly with time, which is confirmed by creep tests where the creep rate decreases very fast.

6 Shear stresses from water flow past a bentonite gel in a fracture

Here the risk of erosion by water flowing past the bentonite penetration front in a fracture is analysed.

If the shear stresses caused by water flowing along a front of a bentonite gel are strong enough the gel may lose material by erosion. However, the flow rate under repository conditions is too low in order to cause such erosion, which will be shown in this chapter.

Figure 6-1 illustrates the fracture. The rectangular fracture is used as a model for the real fracture to calculate the shear stress on the clay. In the rectangular fracture, that stress is represented by the shear stress on the short side at $y = -w/2$ in limit of $w \gg h$.

The velocity field $v_x(y,z)$ for the rectangular fracture in Figure 6-1 can be written (Bruus 2014)

$$v_x(y,z) = \frac{4h^2 \Delta P}{\pi^3 \eta L} \sum_{n,\mathrm{odd}}^{\infty} \frac{1}{n^3} \left[1 - \frac{\cosh n\pi\, y/h}{\cosh n\pi\, w/2h} \right] \sin n\pi \frac{z}{h} \qquad \text{(Equation 6–1)}$$

where η is the viscosity, ΔP is the water pressure difference over the length L.

If we first assume a wide fracture (w → ∞ in Figure 6-1) equivalent to two parallel planes, and the no-slip condition is valid at the fracture walls, then the wall shear stress, τ_z, is defined as

$$\tau_z = \eta \left. \frac{\partial v_x}{\partial z} \right|_{z=0} = \eta \left. \frac{\partial v_x}{\partial z} \right|_{z=h} \qquad \text{(Equation 6–2)}$$

The no-slip condition ($v_x(z = 0) = v_x(z = h) = 0$) implies a parabolic velocity profile

$$v_x(z) = \frac{1}{2\eta} \frac{\Delta P}{L} z(h - z) = \frac{6\langle v_x \rangle}{h^2} z(h - z) \qquad \text{(Equation 6–3)}$$

where $\langle v_x \rangle$ denotes the average velocity in the fracture. Thus the fracture wall shear stress is

$$\tau_z = \frac{1}{2} \frac{\Delta P}{L} h = \eta \frac{6\langle v_x \rangle}{h} \qquad \text{(Equation 6–4)}$$

One may also derive Equation 6–4 from Equation 6–1 by assuming $w \gg h$ and then evaluate $dv_x(0,z)/dz$. To arrive at the final expression one also needs the relation $\sum_1^\infty 1/n^2 = \pi^2/6$.

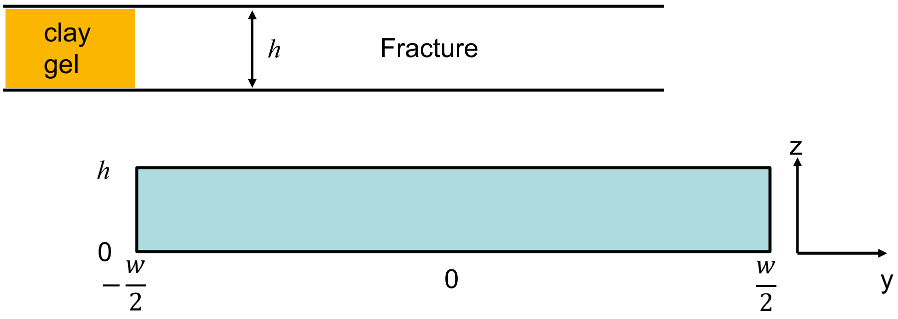

Figure 6-1. *Top: Illustration of non-swelling clay gel in a fracture of aperture h. The water flow in the fracture is assumed to be in the x-direction, i.e. perpendicular to the view. Bottom: Schematic of a rectangular fracture of aperture h and width w. The water flows in the x-direction with velocity* $v_x(y,z)$. *It is assumed that* $h < w$.

With $\eta = 1 \times 10^{-3}$ Pa × s (viscosity of water), $h = 100$ µm, and $\langle v_x \rangle = 1$ m/h $= 2.8 \times 10^{-4}$ m/s which is a rather high velocity, Equation 6–4 gives $\tau_z = 0.02$ Pa. Thus the shear stresses on the fracture walls and bentonite front are much smaller than the measured yield strength of Wy-Na gels at the CCC. This is consistent with the result that no erosion of Wy-Na was detected in artificial-fracture experiments when the flowing solution had NaCl concentration above the CCC (Hedström et al. 2016).

Equation 6–4 gives the shear stress on the fracture, while we actually are interested in the shear stress on the clay surface, which we may assume being perpendicular to the fracture. The maximum value is obtained at the midplane in the fracture ($z = h/2$) so one must evaluate

$$\tau_y = \eta \left. \frac{\partial v_x\left(y, \frac{h}{2}\right)}{\partial y} \right|_{y=-\frac{w}{2}} \qquad \text{(Equation 6–5)}$$

By inserting Equation 6–1 in Equation 6–5 one can show that $\tau_y < \frac{3}{4}\, \tau_z$, thus the shear stress from Equation 6–4 represents an overestimate of the shear stress acting on the clay. Thus we may conclude that the gel can withstand the shear stress from the flowing water by a large margin.

7 Conclusions

Swelling of bentonite into a fracture that takes place in a groundwater that has a NaCl concentration above the critical coagulation concentration (CCC) has been analysed. The processes involved when bentonite swells until it becomes a non-swelling gel, which it will when the groundwater is above the CCC, have been analysed. Since the problem of colloid erosion is largest for homoionic Na-montmorillonite, limits have been determined for such types of systems. CCC for homoionic Na-montmorillonite (Wy-Na) extracted from MX-80 is 20 mM NaCl(aq). At this NaCl concentration the swelling stops at a clay concentration of approximately 60 g/L.

In order to estimate the swelling of bentonite in a fracture we need to know

- the swelling pressure and swelling behaviour of the bentonite at clay concentrations higher than 60 g/L,
- the resistance against penetration that is caused by shear resistance or friction in the bentonite and between the bentonite and the fracture surfaces and
- the shear strength of the non-swelling gel at 60 g/L.

In addition we need to have a calculation tool for estimating the penetration depth and the swelling pressure and density loss along the fracture. Also knowledge of the long term behaviour of the gel is needed. These matters have been investigated and analysed in this report.

The common tests and expressions of swelling pressure have concerned higher densities than the density of a bentonite gel near the CCC. In order to include lower densities, DLVO theory and DLVO theory combined with literature swelling pressure data at low clay concentrations have been used to derive expressions of swelling pressure vs dry density. The DLVO pressure at 60 g/L and 20 mM NaCl is virtually negligible while the expression that also incorporates experimental information give a pressure of 1.1 kPa. Since the clay turns into a non-swelling gel at the CCC at 60 g/L the pressure is explicitly set to 0 for lower clay concentrations.

Another issue concerns the shear strength of the non-swelling gel. With rotating-vane rheometry the shear strength at CCC and 60 g/L was determined to be 40 Pa for a gel that has been left undisturbed for 44 h. It was shown that this value is far higher than expected shear stresses from flowing water in a fracture. Thus, when a gel is formed no erosion is expected. This also agrees with that no flow-induced erosion was observed in previous tests in artificial fractures under conditions above CCC.

Theory is developed for the bentonite penetration into a horizontal fracture. The penetration depth is analysed in terms of the equilibrium situation where the swelling is completed, and the swelling pressure is balanced by the friction against the fracture walls. There are several ways of estimating the friction angle at the low dry densities relevant for the non-swelling gel. Depending on the approach taken and the swelling pressure chosen the evaluated friction angles show large variations, 0.5 to 30°. However, by using these large variations in the sensitivity analyses we were able to show that the penetration into a 100 µm wide fracture is anyway limited to <8 0 mm at the lowest friction angle. Comparison between theory and experimental swelling of Wy-Na into a 120 µm fracture gives best agreement for the highest friction angle, 30° which gave a penetration depth in the vicinity of 1 mm. Thus, we can conclude that above the CCC the bentonite swelling into fractures is limited to distances very much smaller than the deposition hole diameter. Other tests above and below CCC have confirmed this conclusion.

The influence of gravity was also studied and shows to be insignificant for the current problem where the salinity is above the CCC. Thus, the analysis performed for horizontal fractures also holds for sloped fractures.

There are numerous examples of measurements of shear resistance in bentonite and between bentonite and a surface. In the report examples are given of both finished and ongoing measurements, which show that complete homogenisation is hindered by frictional stresses in the bentonite and between the bentonite and the confining surfaces. Ten long term tests in long tubes are ongoing with low density bentonite in one half of the tube in contact with high density bentonite in the other half.

The longest test has been running for 5 years. One test was terminated after two years. Both show a remaining density gradient in the axial direction that corresponds to an average friction angle between the bentonite and the tube of about 7 degrees. The tests will run for many years and be terminated and sampled successively.

Creep tests with constant deviatoric stress applied on a bentonite specimen in a triaxial apparatus show that the creep rate decreases very fast and cannot give rise to large deformations and loss of shear resistance.

In conclusion this report shows that there is a shear resistance or a friction in bentonite and between bentonite and confining surfaces that hinders bentonite in a groundwater with salinity above the CCC to swell deeply into any fracture. In addition the report shows that the strength of the non-swelling bentonite gel that is formed at the swelling front is with large margin high enough to withstand both the gravitational forces and the erosional forces caused by ground water flow past the swelling front.

References

SKB's (Svensk Kärnbränslehantering AB) publications can be found at www.skb.com/publications.

Abend S, Lagaly G, 2000. Sol–gel transitions of sodium montmorillonite dispersions. Applied Clay Science 16, 201–227.

Baik M-H, Cho W-J, Hahn P-S, 2007. Erosion of bentonite particles at the interface of a compacted bentonite and a fractured granite. Engineering Geology 91, 229–239.

Birgersson M, Börgesson L, Hedström M, Karnland O, Nilsson U, 2009. Bentonite erosion Final report. SKB TR-09-34, Svensk Kärnbränslehantering AB.

Bruus H, 2014. Governing equations in microfluidics. In Laurell T, Lenshof A (eds). Microscale acoustofluidics. Cambridge: Royal Society of Chemistry, 1–28.

Börgesson L, 2001. Äspö Hard Rock Laboratory. Compilation of laboratory data for buffer and backfill materials in the Prototype Repository. SKB IPR-01-34, Svensk Kärnbränslehantering AB.

Börgesson L, Hökmark H, Karnland O, 1988. Rheological properties of sodium smectite clay. SKB TR 88-30, Svensk Kärnbränslehantering AB.

Börgesson L, Johannesson L-E, Sandén T, Hernelind J, 1995. Modelling of the physical behaviour of water saturated clay barriers. Laboratory tests, material models and finite element application. SKB TR 95-20, Svensk Kärnbränslehantering AB.

Börgesson L, Hernelind J, Åkesson M, 2018. EBS TF – THM modelling. Homogenisation task. SKB P-18-05, Svensk Kärnbränslehantering AB.

Dueck A, Nilsson U, 2010. Thermo-hydro-mechanical properties of MX-80. Results from advanced laboratory tests. SKB TR-10-55, Svensk Kärnbränslehantering AB.

Dueck A, Börgesson L, Johannesson L-E, 2010. Stress-strain relation of bentonite at undrained shear. Laboratory tests to investige the influence of material composition and test technique. SKB TR-10-32, Svensk Kärnbränslehantering AB.

Dueck A, Goudarzi R, Börgesson L, 2011. Buffer homogenisation, status report. SKB TR-12-02, Svensk Kärnbränslehantering AB.

Dueck A, Goudarzi R, Börgesson L, 2014. Buffer homogenisation, status report 2. SKB TR-14-25, Svensk Kärnbränslehantering AB.

Dueck A, Goudarzi R, Börgesson L, 2015. Buffer homogenisation, status report 3. SKB TR-16-04, Svensk Kärnbränslehantering AB.

Dueck A, Goudarzi R, Börgesson L, 2017. Buffer homogenisation, status report 4. SKB TR-17-04, Svensk Kärnbränslehantering AB.

Eriksson R, Schatz T, 2015. Rheological properties of clay material at the solid/solution interface formed under quasi-free swelling conditions. Applied Clay Science 108, 12–18.

Evans D F, Wennerström H, 1999. The colloidal domain: where physics, chemistry, biology, and technology meet. 2nd ed. New York: Wiley-VCH.

Goh R, Leong Y-K, Lehane B, 2011. Bentonite slurries–zeta potential, yield stress, adsorbed additive and time-dependent behaviour. Rheologica Acta 50, 29–38.

Graham J, Oswell J M, Gray M N, 1992. The effective stress concept in saturated sand-clay buffer. Canadian Geotechnical Journal 29, 1033–1043.

Harrington J F, Birchall D J, 2007. Sensitivity of total stress to changes in externally applied water pressure in KBS-3 buffer bentonite. SKB TR-06-38, Svensk Kärnbränslehantering AB.

Hedström M, Ekvy Hansen E, Nilsson U, 2016. Montmorillonite phase behaviour Relevance for buffer erosion in dilute groundwater. SKB TR-15-07, Svensk Kärnbränslehantering AB.

Johannesson L-E, Sandén T, Dueck A, 2008. Deep repository – engineered barrier system. Wetting and homogenization processes in backfill materials. Laboratory tests for evaluating modeling parameters. SKB R-08-136, Svensk Kärnbränslehantering AB.

Karnland O, Muurinen A, Karlsson F, 2005. Bentonite swelling pressure in NaCl solutions – Experimentally determined data and model calculations. In Alonso E E, Ledesma A (eds). Advances in understanding engineered clay barriers. London: Taylor & Francis, 241–256.

Karnland O, Olsson S, Nilsson U, 2006. Mineralogy and sealing properties of various bentonites and smectite-rich clay material. SKB TR-06-30, Svensk Kärnbränslehantering AB.

Martin C, Pignon F, Magnin A, Meireles M, Lelièvre V, Lindner P, Cabane B, 2006. Osmotic compression and expansion of highly ordered clay dispersions. Langmuir 22, 4065–4075.

Michot L J, Bihannic I, Porsch K, Maddi S, Baravian C, Mougel J, Levitz P, 2004. Phase diagrams of Wyoming Na-montmorillonite clay. Influence of particle anisotropy. Langmuir 20, 10829–10837.

Mourchid A, Delville A, Lambard J, LeColier E, Levitz P, 1995. Phase diagram of colloidal dispersions of anisotropic charged particles: equilibrium properties, structure, and rheology of laponite suspensions. Langmuir 11, 1942–1950.

Quirk J P, Marčelja S, 1997. Application of double-layer theories to the extensive crystalline swelling of Li-montmorillonite. Langmuir 13, 6241–6248.

Ruths M, Israelachvili J N, 2008. Surface forces and nanorheology of molecularly thin films. In Bhushan B (ed). Nanotribology and nanomechanics. Berlin: Springer, 417–515.

Secor R B, Radke C J, 1985. Spillover of the diffuse double layer on montmorillonite particles. Journal of Colloid and Interface Science 103, 237–244.

Svoboda J, 2013. The experimental study of bentonite swelling into fissures. Clay Minerals 48, 383–389.

Verwey E J W, Overbeek J T G, 1948. Theory of the stability of lyophobic colloids: the interaction of sol particles having an electric double layer. New York: Elsevier.

Zhang F, Low P F, Roth C B, 1995. Effects of monovalent, exchangeable cations and electrolytes on the relation between swelling pressure and interlayer distance in montmorillonite. Journal of Colloid and Interface Science 173, 34–41.

Åkesson M, Börgesson L, Kristensson O, 2010. SR-Site Data report, THM modelling of buffer, backfill and other system components. SKB TR-10-44, Svensk Kärnbränslehantering AB.

Appendix 1

Equilibrium after swelling into the slot without considering in-plane stresses

Force equilibrium in radial direction:

$$\sigma \cdot 2\pi r a - (\sigma + d\sigma)2\pi(r + dr)a = \left[\pi(r + dr)^2 - \pi r^2\right]\left(\sigma + \frac{d\sigma}{2}\right)\cdot \tan\phi \cdot 2$$

$$-\sigma dr - r d\sigma = \sigma r dr \cdot \frac{2\tan\phi}{a}$$

$$-\frac{dr}{r} - \frac{d\sigma}{\sigma} = dr\frac{2\tan\phi}{a}$$

Integrating from r_1 to a specified maximum distance between the holes r_2:

$$-\int_{\sigma_1}^{\sigma_2}\frac{d\sigma}{\sigma} = \int_{r_1}^{r_2}\frac{dr}{r} + \frac{2\tan\phi}{a}\int_{r_1}^{r_2} dr$$

$$\ln\sigma_1 - \ln\sigma_2 = \ln\frac{r_2}{r_1} + (r_2 - r_1)\frac{2\tan\phi}{a}$$

$$\ln\sigma_2 = \ln\sigma_1 - \ln\frac{r_2}{r_1} - \frac{r_2 - r_1}{a}\cdot 2\tan\phi$$

For a more general case, see Åkesson et al. (2010).

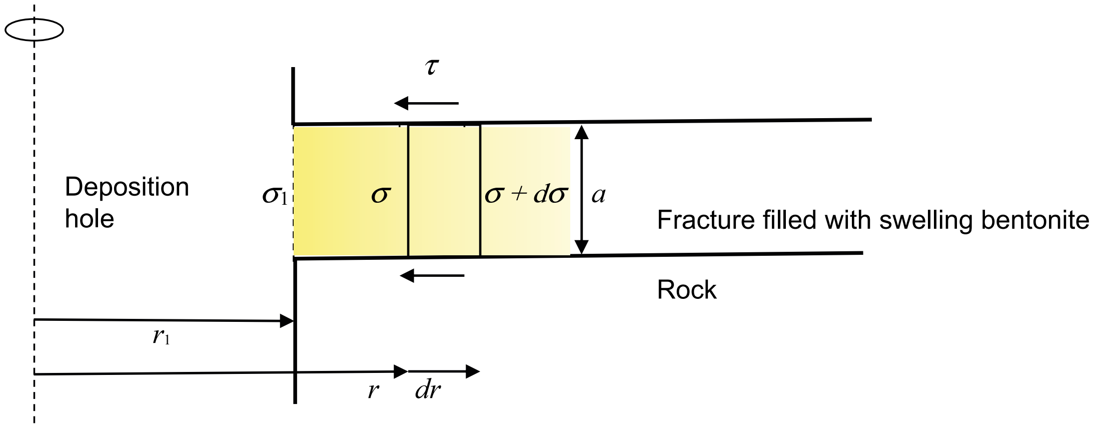

Figure A-1. *State of equilibrium of an infinitesimal part of bentonite dr after swelling into a fracture where*

r_1 = deposition hole radius
a = fracture aperture
σ_1 = swelling pressure at the deposition hole wall
σ = swelling pressure at the distance r–r_1 into the fracture
$d\sigma$ = change in swelling pressure at the increased distance dr
τ = shear stress at the fracture wall

Arkitektkopia AB, Bromma, 2018

SKB is responsible for managing spent nuclear fuel and radioactive waste produced by the Swedish nuclear power plants such that man and the environment are protected in the near and distant future.

skb.se

SVENSK KÄRNBRÄNSLEHANTERING